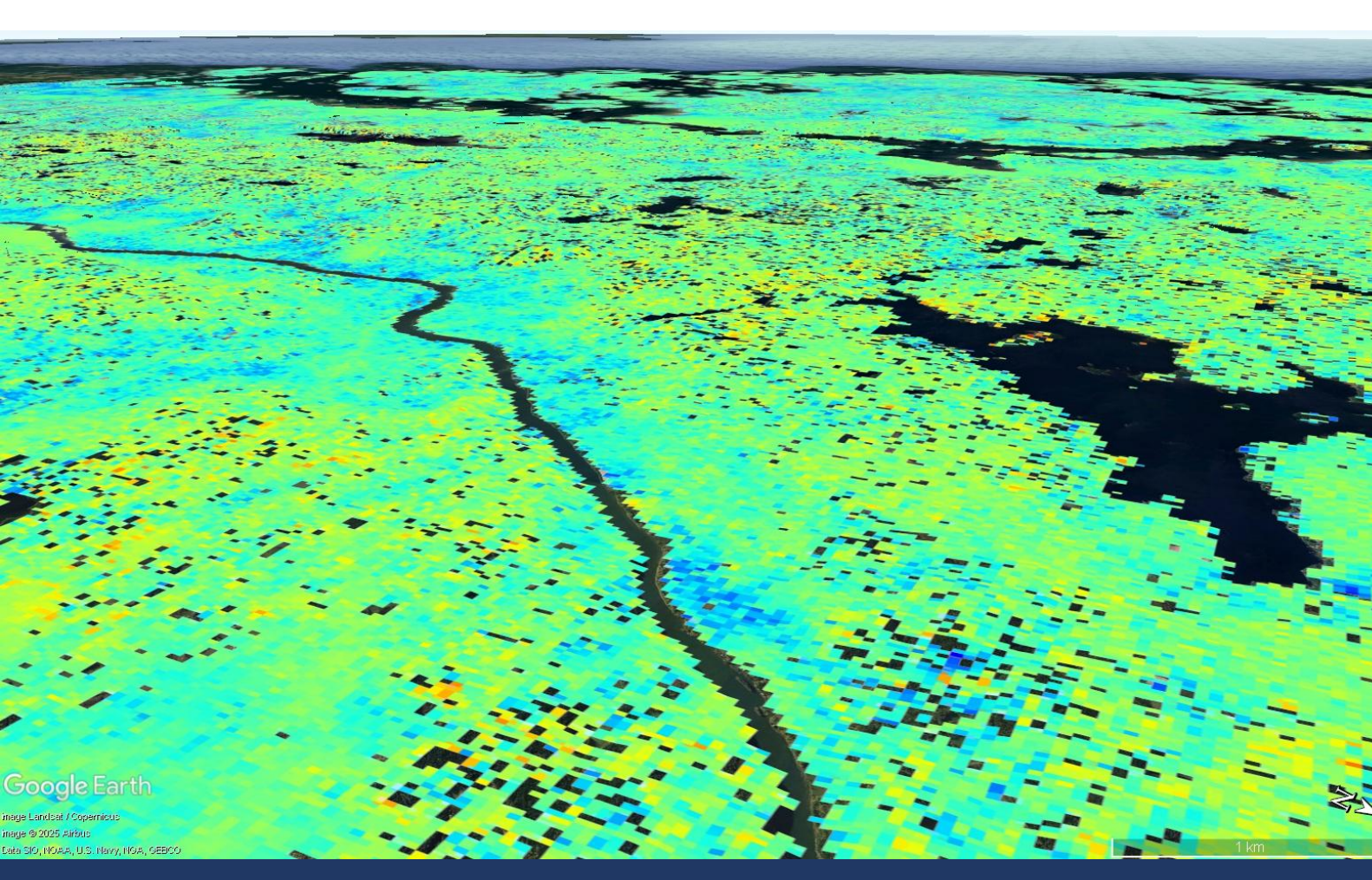


Monitoring Landslide Risk in Västra Götaland: Assessing Surface Deformation Using SBAS InSAR Time Series Analysis

Alexandra Björnfot



Monitoring Landslide Risk in Västra Götaland: Assessing Surface Deformation Using InSAR SBAS Time Series Analysis

Alexandra Björnfot

Department of Physical Geography

Course name: GE9009 Degree project in Physical Geography and

Quaternary Geology Series: NKA 402

Name of programme: Master's Programme in Geomatics with

Remote sensing and GIS (120 hp)

Spring term 2025

Supervisors: Ian Brown (Stockholm University) & Sofia Åsberg

(Trafikverket)

Examiner: Gustaf Hugelius © Alexandra Björnfot

Cover: SBAS Results, Google Earth, Alexandra Björnfot



Abstract

This study evaluates the use of Small Baseline Subset (SBAS) InSAR for monitoring ground deformation in landslide-prone areas, with parts of Västra Götaland, Sweden, as a case study. The main objectives are to examine the detection and monitoring of surface displacement with SBAS-InSAR time-series analysis, to identify limitations of the method, and to determine its potential usefulness in improving landslide risk mapping. Sentinel-1 C-band data (2017–2021) were acquired via ASF HyP3 and processed in MintPy on ASF's OpenSARLab, producing ascending and descending interferogram stacks with a 6-day temporal baseline (with a seasonal gap over the winter months) and a 200 m perpendicular threshold. The two geometries were averaged to reduce line-ofsight (LOS) bias and mitigate geometric distortions such as layover and shadow. Zonal statistics of soil data revealed four main soil types; post-glacial fine sediment, clay-silt sediment, sandy sediment, and glacial sediment where subsidence were greatest. A slope analysis revealed that flatter areas experienced more subsidence than steeper terrain. Comparisons with the Swedish Geological Survey's national susceptibility map revealed strong spatial agreement in high-risk areas, while SBAS also detected previously unmapped subsidence areas. Analysis of the Göta River valley, one of Sweden's most vulnerable areas, was also made that exposed SBAS limitations: its resolution and coherence constraints mean it cannot replace field surveys, but it effectively detects areas needing further investigation. The error and coherence analysis support the overall reliability of the time series. These results demonstrate the usefulness of SBAS-InSAR as a complementary tool for landslide monitoring and risk assessment at a regional scale.

Keywords

SBAS; InSAR; Surface deformation; Subsidence; Landslide susceptibility; Landslide monitoring; Sentinel-1; SAR; Västra Götaland.

Glossary

ASF – Alaska Satellite Facility

DEM – Digital Elevation Model

EGMS – European Ground Motion Service

ESA – European Space Agency

GIS – Geographic Information System

GNSS - Global Navigation Satellite System

HyP3 – Hyperspectral and SAR Processing Platform

InSAR – Interferometric SAR

LOS - Line-of-Sight

LSM – Landslide Susceptibility Mapping

MSB – Myndigheten för Samhällsskydd och Beredskap (Swedish Civil Contingencies Agency)

PS – Persistent Scatterer

PSI – Persistent Scatterer Interferometry

SAR – Synthetic Aperture Radar

SBAS - Small Baseline Subset

SGI – Statens Geotekniska Institut (Swedish Geotechnical Institute)

SGU – Sveriges Geologiska Undersökning (Geological Survey of Sweden)

SLC – Single Look Complex

 $SMHI-S veriges\ meteorologiska\ och\ hydrologiska\ institut\ (Swedish\ Meteorological\ and\ Hydrological\ Institute)$

Table of Contents

G	ilossary	,	3
1	Intro	duction	1
	1.1	Nim	4
2	Back	ground	4
	2.1 L	andslides	4
	2.2	SAR	4
	2.2.1	Sentinel-1 mission	5
	2.3	SAR and its applications	6
	2.4 F	Remote sensing in Sweden	7
	2.5 L	andslide Susceptibility Mapping in Sweden	7
	2.5.1	Soil maps	7
	2.5.2	National Landslide Susceptibility map	8
	2.5.3	Göta River Landslide Risk Map	10
3	Meth	odology	11
	3.1	Study Area	11
	3.1.1	Geological and Geomorphological Characteristics	12
	3.1.2	Climate	12
	3.2	Pata Acquisition and Preparation	12
	3.2.1	Sentinel-1 SAR Data	12
	3.2.2	Downloaded Data	13
	3.2.3	GNSS Data	14
	3.3 \	Vorkflow and Analysis	15
	3.3.1	InSAR Data Processing	15
	3.3.2	Error Analysis	17
	3.3.3	GNSS Validation	
	3.3.4	ArcGIS PRO Analysis	17
4	Resu	lts	19
	4.1	Surface Deformation Overview	19
	4.1.1	Velocity analysis	19
	4.1.2	Cumulative Displacement Analysis	20
	4.2	Comparison with Existing Landslide Assessments	20
	4.2.1	National landslide susceptibility map	20
	4.2.2	Göta River Valley Risk map	21
	4.3 H	listorical Landslides Analysis	23
	4.4 F	Railway Deformation Analysis	23
	4.5 E	rror Analysis	25

4	.6 GNS	S Validation	. 27
5	Discuss	ion	28
5	5.1 Mair	n Findings	. 28
	5.1.1	Ground Deformation Patterns	. 28
	5.1.2	Susceptibility and Risk maps	. 29
	5.1.3	Historical landslides	. 30
	5.1.4	Railways	. 30
	5.1.5	Error Analysis	. 31
	5.1.6	GNSS Validation	. 31
5	5.2 Met	nod - Reflections and Limitations	. 32
	5.2.1	InSAR processing and workflow	. 32
	5.2.2	Temporal and Seasonal Gaps	. 33
	5.2.3	Interpreting Velocity vs. Displacement	. 33
	5.2.4	Averaging of Ascending and Descending Orbits	. 33
5	5.3 Poss	sible Improvements and Future Studies	. 34
	5.3.1	Separating Vertical and Horizontal Components	
	5.3.2	Sensor Selection and Resolution	
	5.3.3 Learning	Integrating InSAR with Susceptibility Mapping and Machine 34	3
	5.3.4	Lessons from Norway's National Monitoring	. 34
6	Conclus	ion	35
Ac	knowled	gement	36
Re	ferences		37
)ata		. 45
Ар	pendix		45
А	ppendix A	: InSAR data overview and SBAS quality assessment	. 45
A	ppendix B	: Supplementary GIS maps and data	. 49

1 Introduction

Landslides are a serious natural hazard that can cause damage to infrastructure, threaten human lives, and impact the environment (Confuorto et al., 2017; Dai et al., 2002; Nikolakopoulos et al., 2023; Ado et al., 2022; Gaidzik & Ramirez-Herrera, 2021; Lee, S. 2019). They happen when a slope's gravitational pull is greater than the material's resistance (Cruden & Varnes, 1996; Shanmugam & Wang, 2015). Understanding the mechanisms and triggers behind them is vital to mitigate their impact as they can result in economic losses, injuries, fatalities, and disruptions to infrastructure (Dai et al., 2002; Ado et al., 2022; Gaidzik & Ramirez-Herrera, 2021). Therefore, determining landslide susceptibility and putting in place efficient monitoring and mitigation strategies are crucial (Confuorto et al., 2017; Highland & Bobrowsky, 2008).

Landslide Susceptibility Mapping (LSM) helps identify areas where landslides are more likely to occur. This is done by analyzing different factors such as geology, topography, hydrology and land cover (Ciampalini et al., 2016). These maps are useful in land-use planning to restrict development in high risk areas and for mitigation measures such as drainage systems or slope stabilization (Dai et al., 2002; Highland & Bobrowsky, 2008).

Geographic Information Systems (GIS) have become a widely used tool for combining geospatial data analysis for factors related to landslide risk (Sarkar & Kanungo, 2004; Ciampalini et al., 2016). In recent years, more advanced models like logistic regression and machine learning have been applied to find patterns in where landslides have occurred in the past, to find patterns for predicting future risk (Shahri et al., 2019). The quality of these models depends on accurate, validated landslide inventories (Erener et al., 2017; Conoscenti et al., 2016).

In recent years, remote sensing techniques such as Synthetic Aperture Radar (SAR) has become increasingly important in landslide research. SAR is an active radar satellite-based system that operates in all weather conditions, including both day and night, making it useful for large-scale monitoring of Earth's surface (Sentiwiki, n.d.). Since the launch of Sentinel-1 in 2014 by the European Space Agency, SAR data has become widely used in research and hazard assessment (Barra et al., 2016; Intrieri et al., 2018).

A commonly used technique is Interferometric SAR (InSAR), which compares radar signals from two or more acquisitions to detect changes in ground elevation (Lu et al., 2007; Yu et al., 2019). One common applied InSAR method is the Small Baseline Subset (SBAS), which processes stacks of SAR interferograms with small spatial and temporal differences to generate a time series of ground movement (Kulsoom et al., 2023; Yalvac, 2020). SBAS can detect slow-moving ground deformation with high accuracy and has been used in several studies to monitor slope activity or update landslide inventories (Confuorto et al., 2017; Ardizzone et al., 2011; Li et al., 2022).

One of the advantages of SBAS is that it can be applied to freely available data, such as Sentinel-1, allowing for large-area coverage and making it suitable for national or regional-scale monitoring (Dai et al., 2002). However, some higher-resolution SAR datasets require commercial access (Barra et al., 2016). SBAS has been used both for early warning and for long-term monitoring of unstable slopes and has been increasingly adopted in landslide studies globally (Ardizzone et al., 2011; Confuorto et al., 2017; Dai et al., 2002; Guzzetti et al., 2009; Kulsoom et al., 2023).

Previous research has shown that SBAS-InSAR works in a variety of environments to detect landslide activity. For example, Rao and Tang (2014) employed the SBAS approach to track deformation along a high-speed railway, demonstrating its value for monitoring infrastructure. In Pakistan, Kulsoom et al. (2023) used SBAS to locate and track landslides along the Karakoram Highway and verify machine learning models used for susceptibility mapping, while Zhang, J. et al. (2022) used SBAS to monitor slope activity along the Lancang River valley in China and showed how the method could improve traditional susceptibility maps by identifying deformation that had not been previously mapped.

In Sweden, Dabiri and Nilfouroushan (2024) used SBAS together with data from the European Ground Motion Service (EGMS) to investigate the 2023 Stenungsund landslide. EGMS provides openly accessible ground motion data across Europe using Persistent Scatterer Interferometry (PSI), which is particularly effective in urban areas where stable reflectors such as buildings are present (Yunjun et al., 2019). SBAS, on the other hand, is more effective for tracking larger-scale movement in natural areas (Li et al., 2022; Zhang, J. et al., 2022). By combining both methods, the authors were able to identify signs of subsidence before the landslide occurred. This case demonstrates how SBAS-InSAR can support long-term monitoring as well as the early detection of slow ground movement, especially when complemented by PSI in built environments (Nikolakopoulos et al., 2023; Dabiri & Nilfouroushan, 2024). Several studies have emphasized that SBAS is capable of identifying subtle ground deformation that may precede landslides, sometimes even before any visible signs are apparent on the surface (Zhang, J. et al., 2022; Nikolakopoulos et al., 2023; Li et al., 2022).

Across Scandinavia, Norway has developed a more advanced national system for landslide monitoring. The Norwegian Water Resources and Energy Directorate (NVE) uses a combination of SBAS-InSAR from Sentinel-1, high-resolution sensors such as TerraSAR-X and COSMO-SkyMed, and ground-based methods to monitor unstable rock slopes and landslide-prone areas (NVE, 2014; NVE, 2015; NVE, 2024). These datasets are integrated into annual hazard map updates which uses InSAR-derived deformation trends. If an area exceeds ±5 mm/year, field investigations are implemented. Monitoring data are shared nationally via the "Naturfareforum" platform, and over 30 active slopes are regularly assessed using this method (NVE, 2016; NVE, 2024).

As climate change and land use continue to increase landslide risks, especially in vulnerable areas, having effective tools for ongoing monitoring are becoming more important (Ado et al., 2022). In Sweden, one of the most vulnerable areas is Västra Götaland County (figure 1), where quick clay, expanding urban development and climate change increase the potential for landslides (SGI, 2012a; SGI & MSB, 2021).



Figure 1. Location of Västra Götaland county in southwestern Sweden outlined in black. Map generated in ArcGIS PRO using a county boundary dataset from Valmyndigheten. (n.d.).

This thesis focuses on a case study in Västra Götaland, including parts of the Göta River valley and the towns of Stenungsund and Lilla Edet, where sensitive clay soils, complex geological conditions, and critical infrastructure are present. The region has been shaped by glacial processes, postglacial sedimentation, and isostatic uplift, all of which have contributed to the formation of clay-rich soils that are prone to slope instability (Andersson-Sköld et al., 2005; 1981; Quigley, 1980; SGI, 2012a). In recent years, infrastructure expansion, erosion, and changing hydrological conditions associated with climate change, increase the potential for landslide risk (SGI & MSB, 2021; Shahri et al., 2019).

1.1 Aim

The main objective of this study is to demonstrate the advantages and limitations of using SBAS-InSAR time series analysis to monitor and understand surface deformation in landslide-prone areas, including parts of infrastructure such as railways, using Västra Götaland, Sweden as a case study. The research questions are as follows:

How can InSAR SBAS time series analysis be used to detect and monitor surface deformation in landslide-prone areas and around vulnerable infrastructure like railways?

Are there limitations of SBAS InSAR in detecting surface deformation?

How can the findings from this study be used to improve risk assessment and monitoring strategies for landslides and infrastructure safety in regions like Västra Götaland?

2 Background

2.1 Landslides

Landslides are a type of mass movement of soil, rock, or debris down a slope when the gravitational force is greater than the resisting force (Cruden & Varnes, 1996). Landslides can occur in diverse environments and can be triggered by natural factors, such as rainfall or earthquakes or human activities such as excavation or land-use change (Confuorto et al., 2017; Highland & Bobrowsky, 2008). A landslide can take several forms, such as slides, falls, flows, or a combination, depending on the material and slope conditions (Highland & Bobrowsky, 2008; Shanmugam & Wang, 2015).

Landslides often fall into categories based on the type of movement and the material involved. Rotational and translational slides, debris flows, earthflows, and rockfalls are typical, with multi-movement landslides including more than one category (Shanmugam & Wang, 2015; Highland & Bobrowsky, 2008). In sensitive clays, retrogressive landslides are especially important. They begin with a small failure at the bottom of a slope and then progress upslope in stages as the newly exposed scarp becomes unstable (Dai et al., 2002; SGI, 2012a). In addition to the sudden and sometimes destructive movements, landslides can develop slowly over time as creep (Zhang, S. et al., 2022). Creep is a gradual, long-lasting ground movement that may not be immediately noticeable but can indicate instability in the slope. It often precedes larger, more rapid failures and is especially relevant in areas where sensitive clays such as quick clay are present (Löfroth et al., 2024).

Landslide impacts can vary from devastating, including destruction of infrastructure and economic loss, to death and long-term disturbance to communities and the environment (Nikolakopoulos et al., 2023). Because of these threats, landslide studies usually focus on understanding failure mechanisms, identifying vulnerable areas, and developing monitoring strategies. Monitoring is effective for detecting slow-moving ground deformation that can show early indications of slope instability before a major event occurs (Löfroth et al., 2024).

2.2 SAR

Synthetic Aperture Radar (SAR) is an active remote sensing system that uses microwave pulses to gather data on the surface of Earth (Sentiwiki, n.d.; NASA, n.d.). The radar

transmits microwave pulses and records the reflected signals, both backscatter amplitude, which relates to surface properties (roughness, slope, moisture), and phase, which encodes the fractional-wavelength shift corresponding to the travel distance between sensor and ground (Hanssen, 2001; Lu et al., 2007; Löfroth et al., 2024).

One of the main advantages of SAR is that it is independent of sunlight and weather conditions, meaning that data can be collected day or night, even under cloudy or rainy conditions (Li et al., 2022; Lu et al., 2007). This is advantageous when monitoring changes in the surface in remote or weather-exposed areas (Intrieri et al., 2018).

The resolution of SAR imagery depends on the radar signals wavelength and on the satellites motion, which collects many echoes along its flight path to form a "synthetic aperture" that gets high resolution without a large physical antenna (NASA, n.d.; SARmap, 2009).

Different radar wavelengths interact differently with the surface. X-band (3.8–2.4 cm) provides high-resolution data but is more sensitive to vegetation cover, making it suitable for urban monitoring (USGS, n.d.; ESA, 2007). C-band (7.5–3.8 cm), used by Sentinel-1, offers a balance between resolution and vegetation penetration, and is commonly used for regional deformation studies (Lu et al., 2007). L-band (30–15 cm) can penetrate deeper and is better suited for maintaining coherence in vegetated areas, since the longer wavelength is less affected by changes in surface properties (Lu et al., 2007; Hoeser, 2018).

As shown in figure 2, the satellite travels along the azimuth direction, while the radar beam looks sideways across the range direction, recording information along its line-of-sight (LOS) (Liang et al., 2021). The radar measures the slant range (R) from the satellite to the ground target, based on the look angle (θ) and the satellite's height (H). These parameters affect how the radar signal interacts with the terrain. On steep slopes, geometric distortions like foreshortening, layover, or shadowing can occur (NASA, n.d.; Sarmap, 2009).

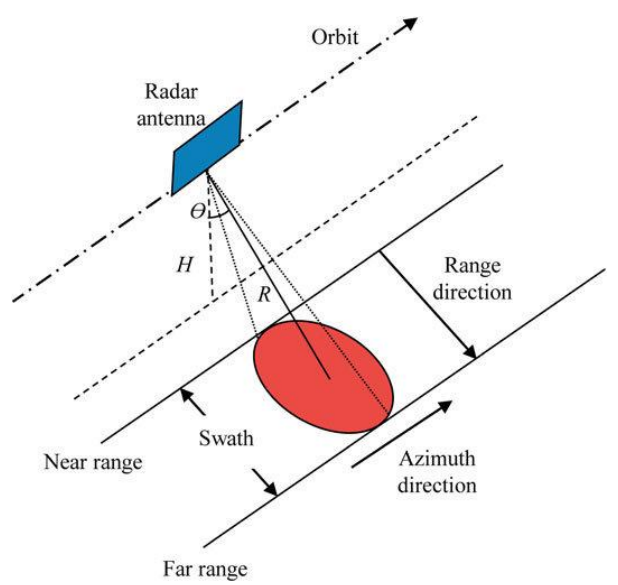


Figure 2. Schematic diagram of a SAR satellite in orbit from Liang et al., (2021). The radar antenna sends pulses toward Earth at a sideways angle (θ), forming a swath on the ground. The satellite moves along the azimuth direction, while signals are received in the range direction. The footprint on the ground is shown in red. R = slant range; H = satellite height.

2.2.1 Sentinel-1 Mission

The Sentinel-1 mission is part of the Copernicus initiative, a program by the European Commission and European Space Agency (ESA) to provide global Earth observation data for environmental and security services (Sentiwiki, n.d.). The mission is a

constellation of two polar-orbiting satellites, which operate in C-band. These satellites are intended to provide open access, all-weather, day-and-night imagery of the Earth's surface (Sentiwiki, n.d.; NASA, n.d.). The Sentinel-1 mission is crucial for land-monitoring, marine-monitoring and emergency response (NASA, n.d.a; ESA, n.d.).

Sentinel-1 operates with a 12-day repeat cycle for one satellite. When both satellites are operational, the mission has a 6-day revisit time, allowing for frequent monitoring of the Earth's surface (Sentiwiki, n.d.; EO Portal, n.d.-a). Since its launch, Sentinel-1A (April 2014) and Sentinel-1B (April 2016) have provided consistent radar data, with Sentinel-1B's mission ending in 2022 due to a technical issue (Sentiwiki, n.d.). The Sentinel-1C satellite launched in December 2024, with Sentinel-1D scheduled for launch in 2025, to ensure continued monitoring (ESA, n.d.).

2.3 SAR and its applications

Interferometric Synthetic Aperture Radar (InSAR) improves the capabilities of SAR by comparing pairs of SAR images over the same area, acquired at different times to detect ground surface displacement (Yu et al., 2019; Armas et al., 2016; Del Soldato et al., 2021). The technique works by analyzing the phase difference between two SAR acquisitions to measure the change in distance between the satellite and the ground, which can indicate movement (Ardizzone et al., 2011; Lu et al., 2007).

InSAR results are typically represented in ground deformation maps that show displacement along the radars line-of-sight (LOS). One commonly used method within InSAR is the Small Baseline Subset (SBAS), which reduces phase decorrelation by selecting SAR pairs with short temporal and spatial baselines (Confuorto et al., 2017; Hanssen, 2001). These selected pairs are combined into a network of interferograms, which are then inverted to produce a time series of surface displacements (Del Soldato et al., 2021; Fabris et al., 2022).

An important factor in InSAR analysis is coherence, which refers to the stability of the radars phase signal between acquisitions (Sarmap, 2021). High coherence means that the surface properties have remained relatively unchanged, allowing for reliable displacement measurements (ESA, 2007). Low coherence may be caused by vegetation, steep terrain, water, snow, or land use changes, all of which introduce noise and reduce reliability (Sarmap, 2021; Hanssen, 2001). A commonly accepted threshold for useful coherence in SBAS time series analysis is around 0.3 for spatial coherence and 0.7 for temporal coherence (Yunjun et al., 2019).

The SBAS approach is particularly useful in detecting long-term, slow ground movement, even in areas where single interferograms are noisy. This makes it suitable for monitoring landslides and slope stability over broad areas (Zhang, J. et al., 2022). InSAR's ability to cover large and often inaccessible regions also makes it an effective tool for detecting deformation where ground investigations may not be possible (Kulsoom et al., 2023; Nikolakopoulos et al., 2023).

Time series analysis allows researchers to track how deformation evolves over time, which is useful for identifying seasonal changes, long-term creep, or potential triggering events such as rainfall or construction (Abdelfattah, 2023; Guzzetti et al., 2009). When combined with other geospatial data, such as digital elevation models or geological maps, InSAR can improve the identification of high-risk zones and refine landslide susceptibility maps (Zhang, J. et al., 2022; Kulsoom et al., 2023).

Another method for measuring ground motion is Persistent Scatterer Interferometry (PSI), which identifies stable, radar-reflective targets like buildings or rock outcrops. PSI is well suited for urban areas and local deformation monitoring, and it is used by the European Ground Motion Service (EGMS) to provide publicly accessible ground motion

data based on Sentinel-1 imagery (ESA, 2007; Yunjun et al., 2019; European Ground Motion Service, n.d.). Unlike SBAS, which is better suited for monitoring large-scale ground deformation over time where there is natural variation (Confuorto et al., 2017; Li et al., 2022), PSI is focus on detecting subtle movements by analyzing stable, reflective surfaces on the ground and is better suited for local deformation and urban areas (ESA, 2007; Confuorto et al., 2017; Yunjun et al., 2019).

2.4 Remote Sensing in Sweden

While remote sensing technologies have long been used by authorities such as Swedish mapping, cadastral and land registration authority (Lantmäteriet), Swedish Geological Survey (SGU), and Swedish Environmental Protection Agency (Naturvårdsverket) mostly through optical imagery, for applications such as land use monitoring, nature protection, and geology (Naturvårdsverket 2024: Lantmäteriet 2024; SGU, 2014; Schoning & Lundqvist, 2020), there is no common use of InSAR as a method of ground movement measurement and infrastructure monitoring. However, radar technology is increasingly used in Sweden in forestry. For example, researchers at the Swedish University of Agricultural Sciences have used Sentinel-1 (C-band), ALOS-2 (L-band) and TanDEM-X (X-band) to map forest structure, biomass and canopy height, for forest inventories, taking use of the advantages of SAR (SLU, 2024).

Even though InSAR is still not part of Swedish standard ground monitoring practice, its benefits has been noted in several studies (Ardizzone et al., 2011; Barra et al., 2016; Confuorto et al., 2017; Nikolakopoulos et al., 2023). InSAR also supports broader goals at the EU level. For example, an initiative promoted by the European Commission since 2023 points out the use of remote sensing technologies to strengthen soil monitoring and improve soil resilience (European Commission, 2023). While that directive mainly concentrates on optical sensors, it also opens up for the use of radar-based methods like InSAR in future land monitoring strategies.

A report from Swedish Transport Administration (Trafikverket, 2022), written by the consulting firm Norconsult, identifies the need for more systematic ground motion monitoring across Sweden's transport network. The report identifies that InSAR can play a role in meeting this need by delivering consistent, large-scale data at relatively low cost. With access to historical Sentinel-1 data dating back to 2015, it becomes possible to track changes over time and compare them with in-situ measurements to support maintenance and risk assessments. According to the report, InSAR should be considered for future monitoring efforts to help detect early signs of instability.

2.5 Landslide Susceptibility Mapping in Sweden

2.5.1 Soil maps

Soil type is one of the most important factors in landslide susceptibility mapping, especially in areas where quick clay may be present (Sarkar & Kanungo, 2004; Lee, S. 2019). In Sweden, soil maps produced by the Geological Survey of Sweden (SGU) are used to assess how different types of ground material affect slope stability and erosion risk. These maps are produced at different scales, 1:25,000 to 1:100,000 (with the lower resolution maps being made from older historical maps that remain in use until updated), using field surveys, soil sampling, laboratory analysis, and GIS-based interpretation (SGU, n.d.-a).

In addition to soil maps, SGU also makes soil depth models and other geological maps, which present the area's geological conditions (SGU, n.d.-b). SGU has since 2021 updated the soil map within the area around Göta River valley to increase accuracy of this vulnerable region (SGU, 2021).

Although older maps created as early as the 1960s may have positional inaccuracies of 25 to 200 meters, they are still used as a foundation in risk mapping (SGU, n.d.-a). SGU continuously updates these maps to improve their precision, ensuring that they remain relevant.

One of the main causes of the high risk for landslides in areas of western Sweden, such as the Göta River valley, is quick clay (SGI, 2012a; SGU, n.d.-c). It's a fine-grained marine clay that seems stable if left undisturbed, but it quickly loses strength and becomes liquid-like under certain circumstances, such as intense rain, construction, or erosion (Andersson-Sköld et al., 2005; Highland & Bobrowsky, 2008). A sudden and disastrous failure may result from this liquefaction. Additionally, creep (a slow, long-term movement of soil that can eventually destabilise slopes and cause failure, particularly in wet conditions) is linked to quick clay (Löfroth et al., 2024). Quick clay was mapped according to the probable locations of brackish or marine environments from glacial and postglacial periods, which allowed for the deposition of fine-grained sediments with quick clay (SGU, 2016).

With funding from the Swedish Civil Contingencies Agency (MSB), SGU, the Swedish Geotechnical Institute (SGI), and the Swedish Transport Administration (Trafikverket) collaborated to test a more detailed approach in 2018. The project aimed to integrate geological, topographical, geophysical, and geotechnical data. Two of the four test areas that were assessed were in the Göta River valley (SGI, 2018; Löfroth et al., 2018). Löfroth et al. (2018) confirm that fall-cone tests on undisturbed samples remain the most reliable indicator for quick clay verification. SGI notes that more thorough examination of site-specific geological and hydrogeological conditions is required for an accurate classification, even though techniques like the Quick Clay Susceptibility Index (QCSI) can offer an initial indication of possible quick clay.

2.5.2 National Landslide Susceptibility map

SGU's product "Riksöversikt finkorniga jordars skredbenägenhet" gives a national overview of the susceptibility of fine-grained soils to landslides throughout Sweden (figure 3) (SGU, 2022a). The mapping uses a general geological assessment of the likely locations of fine-grained sediments, historical landslides, and soil type (SGU, 2022a). However, it cannot account for localized changes such as construction, erosion or stabilization measures (SGU, 2022a).

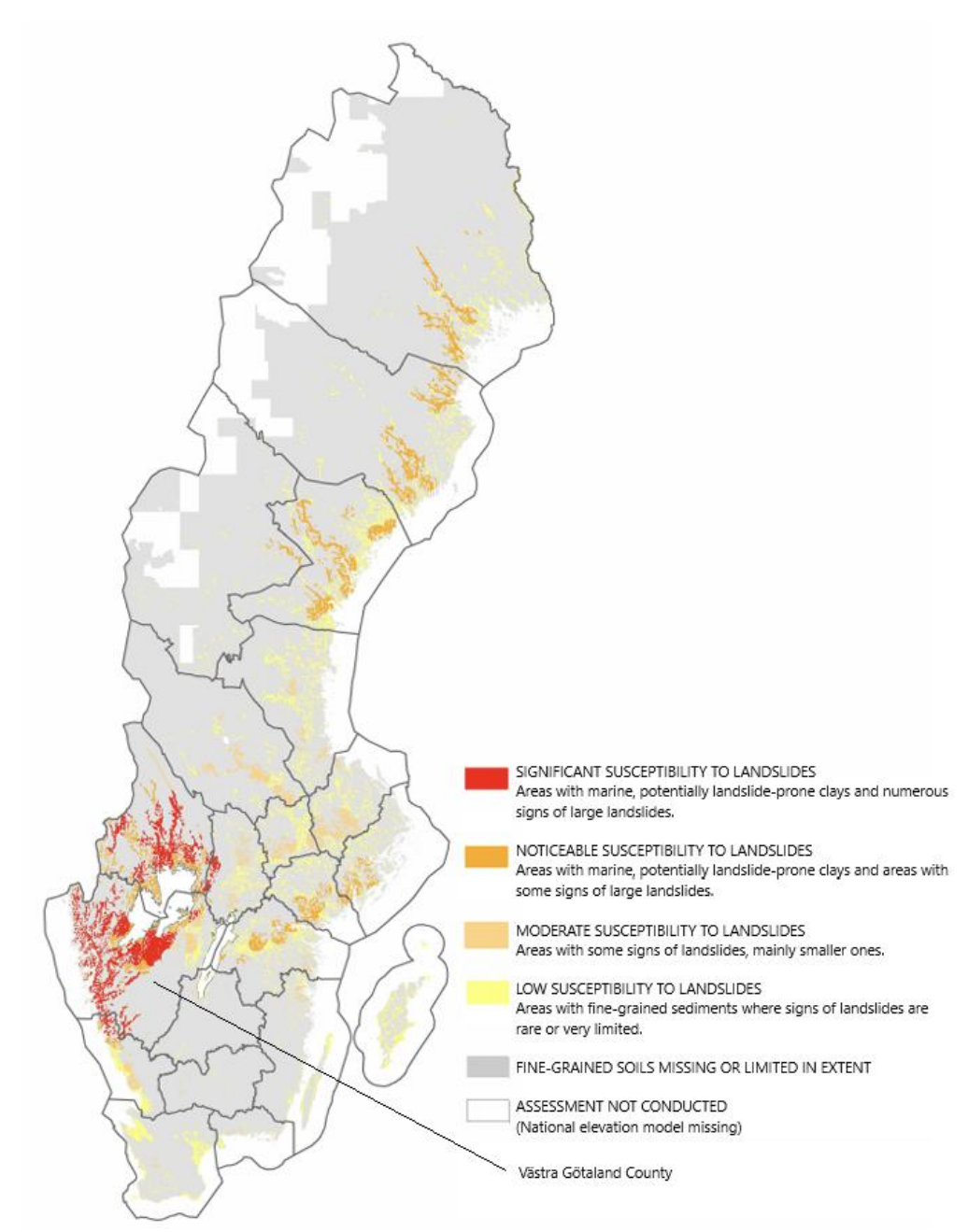


Figure 3. Landslide susceptibility map of Sweden based on SGU (2022a), divided into four risk categories, from significant (red) to low (yellow). The map has been modified to translate the legend to English and to highlight the extent of Västra Götaland County.

SGI released "Vägledning 6" in 2023, a national guideline for mapping the risk of landslides in clay-rich soils. The guidelines describe how preliminary risk areas are identified using base data, including SGU's soil type maps, known landslide scars, and terrain features like ravines. Before risk classification, new mapping is advised if geological data is missing or out-of-date. The use of "typområden" (terrain units), or regions with comparable geological and morphological characteristics, were introduced to aid in the planning of field research and geotechnical drilling.

SGI's guidance report "Kartunderlag om ras, skred och erosion" (2025), which describes how to work with landslide risk mapping in Sweden, provides a more thorough approach. The report mentions the importance of integrating data from various sources, such as SGU, Swedish Meteorological and Hydrological Institute (SMHI), and Lantmäteriet (SGI, 2025).

The following are a few of the primary datasets that the report highlights:

- Field observations and geotechnical borehole data, which provide direct information about soil layers and properties that are important for evaluating slope stability and material strength (SGI, 2025).
- Geological maps and soil depth models from SGU, used to understand surface composition and areas more prone to erosion or failure (SGI, 2025).
- Elevation data from Lantmäteriet, such as the national elevation model, which is important for calculating slope angles and identifying terrain features relevant to landslide formation (SGI, 2025).
- Climate and rainfall data from SMHI, including analyses of extreme weather events, used to assess how rainfall and changing hydrological conditions may influence landslide risk (SGI, 2025).

These datasets are available as GIS layers, which allows for spatial analysis and modeling to assess landslide risk. The report emphasizes the significance of using in-situ validation to verify the mapping (SGI, 2025).

2.5.3 Göta River Landslide Risk Map

Over time, initiatives to improve Västra Götalands landslide risk mapping have been ongoing. One of Sweden's most vulnerable areas to landslides is the Göta River valley, where multiple landslides have damaged communities, roads, and railroads (Alén et al., 2000). SGI has monitored the area since the 1960s due to the increasing expansion of infrastructure and the need for a better understanding of slope stability (Alén et al., 2000).

Alén et al. (2000) classified the area into four classes according to slope stability and the possible outcomes of their early landslide risk assessment. Their approach was based on statistical estimates, field surveys, and the interpretation of aerial photos and geotechnical investigations. Although helpful for broad evaluations, it did not completely take future climate-related hazards into consideration.

In 2009, SGI was assigned by the Swedish government to carry out a more detailed risk mapping of the Göta River valley that took the effects of climate change into account (SGI, 2012a). The new assessment, presented in "Landslide risks in the Göta River valley in a changing climate," took updated geotechnical investigations, soil and bedrock maps, digital elevation models, bathymetry, slope stability calculations, and climate projections from SMHI into consideration (SGI, 2012a; SGI, 2012b). Due to the close proximity of important transport infrastructure, Trafikverket inputs were included (SGI, 2012a).

A risk matrix comprising five probability classes and five consequence classes was introduced as one of the improvements in the 2012 study. This allowed areas to be classified as low, medium, or high risk (SGI, 2012a). The consequences were also estimating costs related to housing, transport, human safety, and environmental damage. The other major shift in the 2012 study was the handling of quick clay and retrogressive landslides. The new method used in-situ methods like cone penetration tests and sounding methods to identify sensitive clay areas. These areas were classified as "secondary" hazard zones (medium or high) as they are prone to retrogressive failure.

3 Methodology

3.1 Study Area

The study area is located in southwestern Sweden, and includes parts of the municipalities Kungälv, Ale, Lilla Edet, Trollhättan and Stenungsund. It also includes parts of the Göta River valley, which stretches from its outlet in Gothenburg to the lake Vänern (SGI, 2012a). This region, located within the Västra Götaland county, is known for its frequent landslides, rockfalls and erosion, which result from a combination of geological, hydrological, and climatic factors (SGI, 2012a). In June 1977, the catastrophic Tuve landslide occurred just north of Gothenburg, claiming 8 lives and destroying over 60 homes (SGI, 1984). This event, triggered by intense rainfall on sensitive clays, remains one of Sweden's most tragic landslides.

This study is a case study focused on these high-risk regions, allowing for in-depth spatial analysis of deformation patterns using SBAS-InSAR. It uses SBAS-InSAR data to map and analyze ground deformation patterns. The selected area (figure 4) includes the Göta River valley, the Stenungsund area and nearby railway lines. These locations were chosen due to known landslide activity, available satellite data from both ascending and descending Sentinel-1 orbits (Zhang, J. et al., 2022; Guzzetti et al., 2009), and the presence of a GNSS station with long-term records that overlap with the SBAS-InSAR observation period (Fabris et al., 2022; Nikolakopoulos et al., 2023; Kulsoom et al., 2023). The final area of interest was defined based on where all datasets intersected, allowing for spatial comparisons and validation of results.

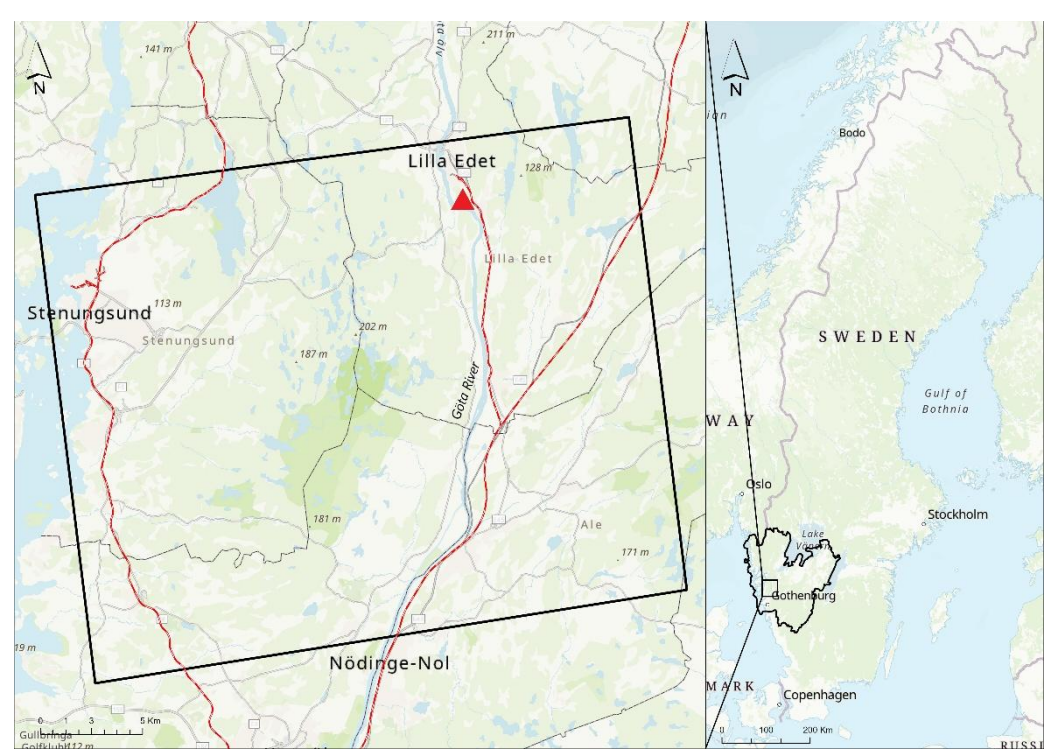


Figure 4. Study area map done in ArcGIS PRO outlined study area in black including the municipalities Kungälv, Stenungsund, Lilla edet, Trollhättan and Ale. The GNSS station used for validation (0LED) is marked with a red triangle and the railway network is marked with red lines.

3.1.1 Geological and Geomorphological Characteristics

The Göta River valley is mainly composed of thick marine clay deposits, often layered with silt and sand (SGI, 2012a). The presence of quick clay, which is known for its high sensitivity to disturbance, is a major contributor to landslide risk in the area (SGI 2012a; SGI, 2018). In addition to sudden failure events, areas with quick clay may also show signs of slow deformation, or creep, which can be influenced by seasonal factors like rainfall or snowmelt (Löfroth et al., 2024).

The valley is underlain by fractured crystalline bedrock, primarily gneiss (SGI, 2012a). Tectonic activity has shaped this bedrock over time, creating fractures that influence surface processes and slope stability. These geological features, combined with steep valley sides and sensitive soil conditions, contribute to the region's high susceptibility to landslides, particularly where quick clay is present (SGI, 2012a; SGI, 2018).

Around Stenungsund, the geology also includes postglacial sediments, mostly sand and silt deposited during deglaciation (SGU, n.d.-a). This, along with steep topography and likelyhood of quick clay deposits, makes the area especially prone to slope instability. The 2023 landslide in Stenungsund is a recent example of this vulnerability, having caused significant damage to infrastructure (Andersson et al., 2023; Shahri et al., 2019).

3.1.2 Climate

The climate in Västra Götaland is influenced by its proximity to the North Sea, resulting in milder winters and cooler summers compared to areas further inland (SGI, 2012a). From 1991 to 2020, February temperatures averaged around -2°C in inland areas and +1°C along the coast, while July temperatures typically reached 18°C, higher elevation areas near lake Vättern experience slightly cooler temperatures around 15-16°C (SMHI, n.d.).

Rainfall is one of the most important climate factors contributing to landslide risk in the area (Andersson-Sköld et al., 2005). The southwestern part of the region typically receives between 1000 and 1200 mm of precipitation each year. The wettest period is usually from September to November, often with over 100 mm of rainfall per month. The driest months are typically February to May, with monthly averages closer to 50 mm (SMHI, n.d.; SGI, 2012a). Snow cover usually lasts 50–60 days per year and accounts for about 15% of annual precipitation (SGI, 2012a).

Climate change has been predicted to likely increase the risk of landslides due to higher precipitation levels. Wetter conditions and more frequent heavy rain events are expected to raise groundwater levels and reduce slope stability, particularly in areas with sensitive soils like quick clay (SGI & MSB, 2021). Without mitigation, landslide risk in the Göta river valley could rise by up to 25% by the year 2100 (SGI & MSB, 2021).

Due to the combination of sensitive clay soils, steep slopes, and increasing rainfall, the region remains one of the most landslide-prone areas in Sweden, with significant consequences for infrastructure and public safety (SGI, 2012a; SGI & MSB, 2021).

3.2 Data Acquisition and Preparation

3.2.1 Sentinel-1 SAR Data

This study used Sentinel-1 C-band SAR data in Single Look Complex (SLC) due to its open-access availability and coverage over the study area. SLC products retain both amplitude and phase information, which is needed for interferogram generation and

time-series analysis (Alaska Satellite Facility, n.d.-a). Data was retrieved from the Alaska Satellite Facility (ASF) through the Hyp3 on-demand product processing platform, which enables the searching, processing, and downloading of preprocessed InSAR products. HyP3 allowed for efficient generation and download of interferometric data stacks, reducing the need for manual processing. For detailed product documentation, see the 'ASF Sentinel-1 InSAR Product Guide' (Alaska Satellite Facility, n.d.-a)

The data covers the time period from 2017 to 2021 and includes both ascending and descending orbit tracks. These years were chosen because they offer consistent coverage from both satellites before Sentinel-1B stopped functioning in 2022.

InSAR processing was done using the Small Baseline Subset (SBAS) method applied through the open-source MintPy software, accessed via Jupyter notebooks on ASF's OpenSARLab platform (ASF OpenSARLab, 2024), which enabled time series analysis of displacement data. This method was chosen due to its ability to generate large-scale displacement data over time, assessing ground deformation (Sarmap, 2021; Ardizzone et al., 2011; Confuorto et al., 2017; Intrieri et al., 2018; Li et al., 2022; Zhang, J. et al., 2022; Yalvac, S. 2020).

Data from both ascending and descending orbits were processed to increase spatial coverage and reduce geometric distortions caused by layover, shadowing and foreshortening (Guzzetti et al., 2009; Lazecky et al., 2016; ESA, 2007). By averaging the velocity results from both geometries, a general deformation pattern can be derived across the study area and improves robustness in places where one geometry may lack readability due to topography or vegetation (ESA, 2007; Ren et al., 2022).

The following parameters were used for Hyp3 processing:

- Temporal Baseline: 6 days was selected to maximize the temporal resolution of the data and minimize the impact of decorrelation over long time intervals (Berardino et al., 2002).
- Perpendicular Baseline: Limited to 200 meters to maintain coherence between interferometric pairs (SARmap, 2021).
- Seasonal Filter: Only acquisitions between March and November were included, avoiding snow-covered periods known to reduce coherence (ESA, 2007). Some additional custom pairs were added manually to fill seasonal gaps.
- Multilooking Parameters: Azimuth and range looks were set to 10x2, resulting in a resolution of 80 meters and pixel spacing of 40 meters (Alaska Satellite Facility, n.d.-a).

197 pairs were downloaded for the ascending dataset and 166 pairs for the descending dataset. The complete list of SBAS processing parameters is provided in Appendix A (table A1).

3.2.2 Downloaded Data

Several external datasets were used to support the SBAS analysis and provide context for interpreting the results and are summarized in table 1. An inventory of historical landslides was obtained from SGIs GIS portal as a shapefile. This dataset includes information about the location, size, and date of some of the events. Within the 2017–2021 timeframe, only one recorded landslide was located in the study area, so the spatial distribution of landslides was the main focus.

A national landslide susceptibility map created by SGU (2022a) was downloaded from SGIs GIS portal. This map categorizes areas into four levels of susceptibility: significant, noticeable, moderate, and low and can be seen in figure 3. It is a broad overview of where fine-grained soils are most prone to slope failure (SGU, 2022a).

A more detailed risk map covering the Göta River valley was also downloaded as a shapefile from SGIs GIS portal. The dataset covers both built and undeveloped areas. It evaluates the risk by combining the probability of landslides with their potential consequences, including human life, infrastructure, and environmental factors (SGI, 2012a). The dataset also includes assessments of secondary effects related to the presence of quick clay and climate change impacts. Landslide probabilities are divided into three classes with two secondary effects for medium and high risk.

To complement the analysis, several geospatial datasets were used to provide context and support interpretation of the InSAR results. A soil type map from SGU (scale 1:25,000–1:100,000) was accessed through the SLU map portal, showing dominant soil types, including postglacial clay and areas with bedrock. A 2-meter resolution Digital Elevation Model (DEM) from Lantmäteriet was used to evaluate terrain slope and landscape features. A national railway layer was also included to identify infrastructure that might be affected by surface deformation.

Together, these geospatial layers helped in interpreting the observed ground movement patterns and relate them to geological conditions, land use, and infrastructure.

Table 1. List of downloaded dataset used for spatial analysis.

Downloaded Datasets		Provided by	Name	
National	Landslide	SGU (2022a)	"Riksöversikt finkortniga jordars	
Susceptibility Map			skredbenägenhet"	
Göta River Valley Risk Map		SGI (2012)	"Skredrisker i Göta Älvdalen"	
Historical Landslides		SGI (2001)	"Inträffade skred, ras och övriga	
			jordrörelser"	
Digital Elevation Model		Lantmäteriet (2016)	"Höjddata Grid 2+"	
Soil types		SGU (2018)	"Jordarter 1:25 000-1:100 000"	
Railway network		Lantmäteriet (2019)	"Fastighetskartan Kommunikation	
			latest, JL"	

3.2.3 GNSS Data

To support the validation of the InSAR results data from the Global Navigation Satellite System (GNSS) was used. GNSS refers to satellite systems that provide global positioning, timing, and navigation data to receivers, which use this information to calculate precise locations (Del Soldato et al., 2021). GNSS is highly accurate, continuous, all-weather, and near-real-time (Jin & Komjathy, 2010).

This technique enables precise determination of position, velocity, and time, giving millimetric accuracy in three-dimensional positioning (East-West, North-South, and vertical components), which makes it useful for confirming ground deformation trends seen in InSAR time series (Del Soldato et al., 2021). The GNSS data were downloaded from the University of Nevada, Reno (n.d.). 0LED was the only station within the study area and time frame that could be used for validation and its location is marked in figure 4.

3.3 Workflow and Analysis

The overall workflow for this study can be divided into two main phases: InSAR processing in ASF's OpenSARLab environment and spatial analysis in ArcGIS Pro and is summarized in figure 5. First, the InSAR pairs from ascending and descending orbits are loaded into OpenSARLab SBAS workflow to generate time-series displacement and mean-velocity maps. Next, these outputs are combined with additional datasets such as DEM, soil types, railway networks, landslide inventories, and susceptibility maps in ArcGIS Pro to perform map overlays, zonal statistics, and final visualization of deformation patterns.

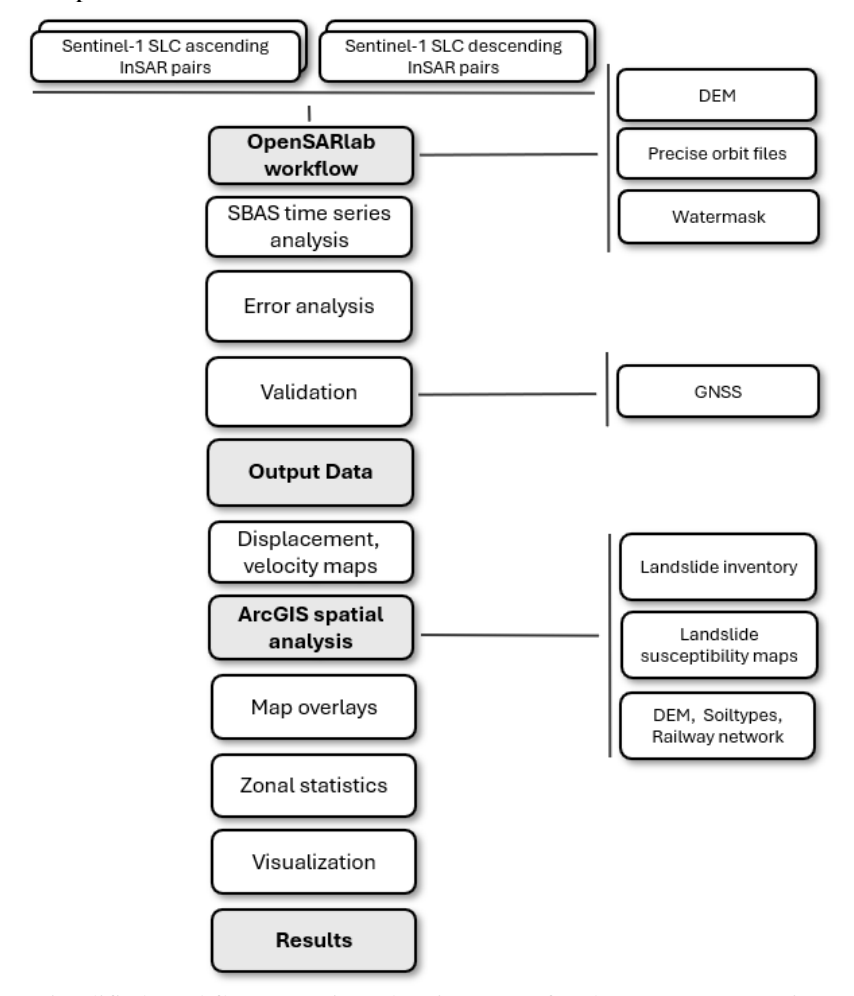


Figure 5. Simplified workflow overview showing steps for the InSAR processing and spatial analysis. Sentinel-1 SAR data were processed through ASF OpenSARLab to generate displacement and velocity maps. These were then integrated with geospatial data in ArcGIS Pro to support landslide risk analysis, zonal statistics, and visualization.

3.3.1 InSAR Data Processing

The SAR scenes used in this project were processed with the SBAS method in ASF OpenSARLab, a cloud-based environment using Python and Jupyter Notebooks (Alaska Satellite Facility, n.d.-b). The processing was based on notebooks publicly available from Lewandowski, A. (2024), who developed a series of step-by-step SBAS workflows for OpenSARLab. These notebooks walk through the process from data handling to time series generation using MintPy. All notebooks are accessible via the official ASF OpenSARLab GitHub repository (ASF OpenSARLab, 2024).

The Jupyter notebooks and steps used in the analysis are summarized in table 2.

Table 2. Summary of Jupyter notebooks used for SBAS time series analysis.

Table 2. Summary of Jupyter notebooks used for SBAS time series analysis.				
Jupyter notebook	Data processing step			
"Install Required Software with Conda"	Set up processing environment inside OpenSARLab			
"Set Up Climate Data Store Access"	Configure access to the Copenicus Climate Data Store so that tropospheric delay could be corrected. Delays in radar signal caused by water vapor and air pressure can interfere with the phase signal and lead to inaccurate displacement results (Afeni & Cawood, 2013). To correct for this, ERA5-Land data was used, which is a reanalysis product that combines weather observations and modeling to give hourly records of atmospheric conditions (Dee et al., 2011; Muñoz Sabater, 2019; Huang et al., 2023).			
"Access HyP3 SBAS Stack"	The pre-processed InSAR stack created in HyP3 was loaded and subset to match the study area. This included the DEM, incidence angle, and azimuth maps needed for MintPy. Since HyP3 data are in UTM format, the stack was reprojected to WGS84 to work properly with MintPy (Yunjun et al., 2019).			
"Load HyP3 SBAS Stack into MintPy"	The interferogram stack generated by HyP3 was loaded into MintPy for time-series analysis. The modify_network step was used to review the interferometric network and apply baseline thresholds for temporal and perpendicular separation. In this case, a few image pairs slightly exceeded the default limits due to data gaps, but no interferograms were removed. A network plot was created to check the overall structure and coverage of the dataset.			
"Configure MintPy Time Series Analysis"	A custom configuration file was written to define the main processing settings. These included using the first acquisition as a reference, enabling tropospheric correction, and letting MintPy choose the reference pixel based on coherence values.			
"Perform MintPy Time Series Analysis"	The full SBAS workflow was run, which included the inversion of interferograms to generate the displacement time series, corrections for tropospheric delay and DEM errors, and the calculation of annual velocity. The outputs consisted of displacement maps, velocity layers, and supporting metadata files. The overall processing steps are illustrated in figure A1 (Appendix A), which shows the steps from interferogram modification to time series generation as defined by Yunjun et al. (2019).			
"Error analysis"	Generate coherence maps and velocity error maps, see section 3.3.2.			

3.3.2 Error Analysis

To assess the reliability of the SBAS results, an error and coherence assessment was done using the Jupyter notebook "Error analysis" from ASF OpenSARLab GitHub repository (ASF OpenSARLab, 2024). This step generated coherence maps and velocity error maps, which helped evaluate the quality of the deformation measurements.

Two types of coherence were calculated:

Spatial coherence refers to how consistent the radar phase is between neighboring pixels. Higher values suggest stable surface conditions and less signal disturbance from terrain or land cover (SARmap, 2009). Low spatial coherence, especially below 0.3, typically indicates unreliable data. These areas often correspond to surfaces with dense vegetation, water bodies, or fast-changing land cover, which can cause the radar signal to lose correlation between acquisitions and reduce the quality of InSAR measurements (Yunjun et al., 2019; Hooper et al., 2004; Hanssen, 2001; Zhang, J. et al., 2022).

Temporal coherence, which reflects the stability of each pixel's phase signal over the entire time series. Low temporal coherence may suggest unreliable data due to temporal decorrelation or atmospheric noise (Hooper et al., 2004). A temporal coherence threshold of 0.7 was applied to mask out unreliable pixels during inversion, ensuring that only stable points were used in the final displacement maps.

To estimate velocity uncertainty, a linear model was fitted to the time series at each pixel. The residuals were used to evaluate how well the data fit the assumed deformation trend. Larger residuals generally indicate greater uncertainty in the estimated velocity, especially in areas with low coherence or atmospheric disturbances (Crosetto et al., 2016).

3.3.3 GNSS Validation

For validation, the SBAS results were compared with GNSS data from the station 0LED located within the study area. The original Python script in the Jupyter Notebook "Error analysis" provided by ASF Opensarlab for GNSS validation, intended to automatically retrieve and compare data, required adjustments, as the automated data extraction failed. Instead, displacement data were manually downloaded using the tenv3 files with 24-hour final solutions. The validation script was adapted using AI-assisted Python scripting to process the downloaded GNSS data and align it with the SBAS results.

GNSS vertical displacement at station 0LED was compared with the SBAS LOS displacement derived from both ascending and descending tracks. Python was used to extract SBAS displacement values from the pixel closest to the GNSS station coordinates (lat 58.114, lon 12.141). Both the SBAS and GNSS displacement time series were resampled to monthly intervals to allow for easier comparison, and the GNSS displacement was referenced to match the SBAS common starting date. This validation process allowed for a comparison of SBAS and GNSS displacement values, helping to identify inconsistencies in the SBAS data (Fabris et al., 2022; Nikolakopoulos et al., 2023; Kulsoom et al., 2023).

3.3.4 ArcGIS PRO Analysis

Data Preparation and Study Area

All datasets were projected to the SWEREF 99 TM coordinate system to ensure alignment and enable spatial analysis (Azarafza et al., 2021). SBAS velocity rasters from ascending and descending orbits were averaged using the Raster Calculator tool to generate a composite velocity map in meters per year. The same was done for the

cumulative displacement raster. The area of overlap between the two orbits defined the final study extent, and all layers were clipped to this extent.

Visualization of SBAS Outputs

The velocity map was visualized using a consistent color scheme, blue for uplift and red for subsidence. The Swipe tool in ArcGIS Pro was used to visually compare the SBAS outputs with other layers, including landslide risk maps and soil maps. The cumulative displacement map was used to assess cumulative displacement over time, but only the velocity map was used for detailed spatial analysis.

Risk Zones and Historical Landslides

The national landslide risk classification map was clipped to the study area, and zonal statistics were used to extract mean SBAS velocities within each of the three mapped classes present in the study area: low, noticeable, and significant susceptibility to landslides. This enabled comparison between areas previously classified as at-risk and the ground deformation patterns observed in the SBAS data.

A more detailed landslide risk layer of the Göta River valley was also included. This map had five categories (low, medium, medium secondary, high secondary, and high), plus areas mapped as bedrock. The velocity raster was clipped to the mapped risk layer, and zonal statistics were used to calculate the average deformation rate for each risk class.

A point layer from SGI's historical landslide database was used. The landslide points were buffered by 100 meters, and zonal statistics were used to calculate the average SBAS velocity in each buffer zone. This analysis checked whether ground motion during the study period coincides with known landslide events.

Infrastructure: Railways

The railway layer was clipped to the study area and buffered by 100 meters to define the zone around the railway. The Extract by Mask tool was used to extract SBAS velocity values within the buffered areas. These values were then classified into four deformation risk categories: low risk for values slower than -0.002 m/year, moderate risk for rates between -0.005 m/year and -0.002 m/year, high risk for -0.010 m/year to -0.005 m/year, and very high risk for any rate exceeding -0.010 m/year.

Soil and Slope Data preparation

Soil type data from SGU (originally 77 classes) were first reclassified into 16 intermediate groups based on sediment origin and material type. These 16 classes were then grouped via zonal statistics of the SBAS velocity to derive a simplified set of four key soil categories coinciding with greatest subsidence (see table B1, Appendix B). A slope raster was generated from a 2-meter DEM and reclassified into slope intervals. Both datasets were clipped to match the study area. Mean SBAS velocities were then calculated for each soil and slope category using the zonal statistics tool to examine trends in ground motion related to terrain and material properties.

4 Results

4.1 Surface Deformation Overview

The SBAS results for the ascending and descending orbits were used to generate both cumulative displacement and average velocity maps. These datasets together forms an overview of ground motion in the study area between March 2017 and November 2021.

4.1.1 Velocity Analysis

The velocity map in figure 6 displays average displacement rates in meters per year during the study period. Values range from approximately -0.072 (subsidence) to +0.049 (uplift) meters per year. To improve reliability and reduce geometric effects, the map is based on the average of both ascending and descending results.

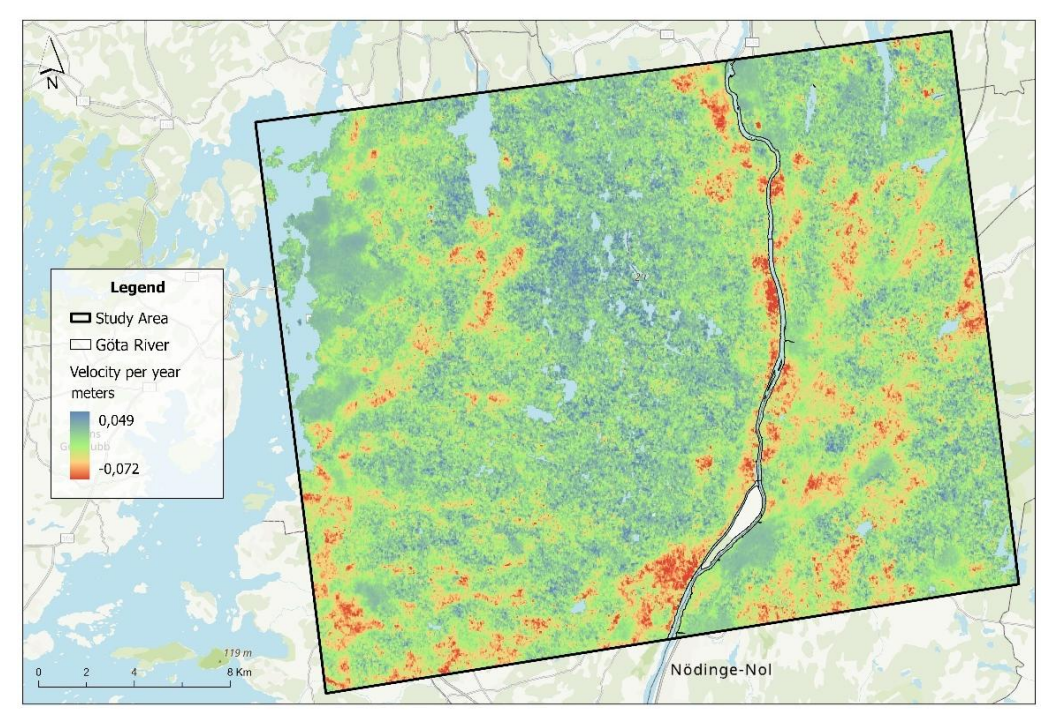


Figure 6. Average surface velocity per year in the study area derived from SBAS using Sentinel-1 data from March 2017 to November 2021. The map displays average ground displacement rates (in meters per year), calculated from the combined ascending and descending track data. Red areas indicate subsidence (negative velocity), while blue-green areas represent uplift or stable conditions (positive velocity). Göta river is marked in a thin black polygon and the thicker black polygon outlines the study area.

Subsidence is most pronounced in the southern and eastern parts of the study area, especially along Göta River, where clusters of red indicate negative deformation rates. In contrast, uplift is primarily observed in the central and northern zones, corresponding to more elevated or geologically stable areas.

Zonal statistics confirm that the highest average subsidence rates occur on Postglacial Fine Sediment, Clay-Silt Sediment, Sandy Sediment, and Glacial Sediment (see table B1, Appendix B, for the full reclassification of soil types). These soil types are concentrated in the western, southern and eastern parts of the study area, particularly along Göta River valley, and has a similar spatial extent as subsidence in the velocity map (see Appendix B, figure B1). Similarly, the slope analysis shows that flatter terrain

have higher subsidence rates, while steeper areas remain relatively stable (see Appendix B, figure B2).

4.1.2 Cumulative Displacement Analysis

The cumulative displacement map was created by averaging the ascending and descending time-series results. It shows the total amount of ground displacement that occurred in the study area between March 2017 and November 2021. Displacement values range from approximately -0.33 meters (subsidence) to +0.23 meters (uplift).

The spatial pattern is similar to the velocity map (figure 6), with uplift mainly in the central parts of the study area, while the southwestern and eastern zones, particularly near the Göta River, show more subsidence.

Because the ascending and descending stacks are referenced to different dates (3 March 2017 and 10 March 2017, respectively), cumulative displacement values can vary due to this reference offset (Yunjun et al., 2019). For that reason, the cumulative map is mainly used for visual interpretation and to understand total ground movement over time.

Since the velocity map shows the general trend across the full time period and isn't influenced by the choice of reference date, it was used as the main layer for the spatial and statistical analysis.

4.2 Comparison with Existing Landslide Assessments

4.2.1 National Landslide Susceptibility map

Within the study area, most of the zones included in the national landslide susceptibility map are marked as having significant susceptibility. To explore how this map compares with the SBAS results, the susceptibility layer was overlaid on the average velocity map (figure 7).

In many cases, there is a clear overlap between zones with mapped susceptibility and areas showing signs of ground motion in the SBAS data, particularly subsidence. Several of the red clusters in the velocity map (subsidence) fall within areas classified as highly susceptible to landslides. This pattern is also supported by the zonal statistics. Areas marked with significant susceptibility had the highest average subsidence at -0.0158 meters per year, and made up nearly all (99.81%) of the mapped zones in the study area. The noticeable class covered a much smaller portion (0.06%) and had an average rate of -0.0075 meters per year. The lowest category showed even smaller deformation (-0.0050 meters/year), but only covered 0.12% of the mapped zones (see Appendix B, figure B3).

Some zones classified as highly susceptible showed uplift trends rather than subsidence during the SBAS period, especially in the western part of the study area. Meanwhile, there were also unmapped areas (outside of the classified zones) where subsidence was detected in the southern parts of the study area.

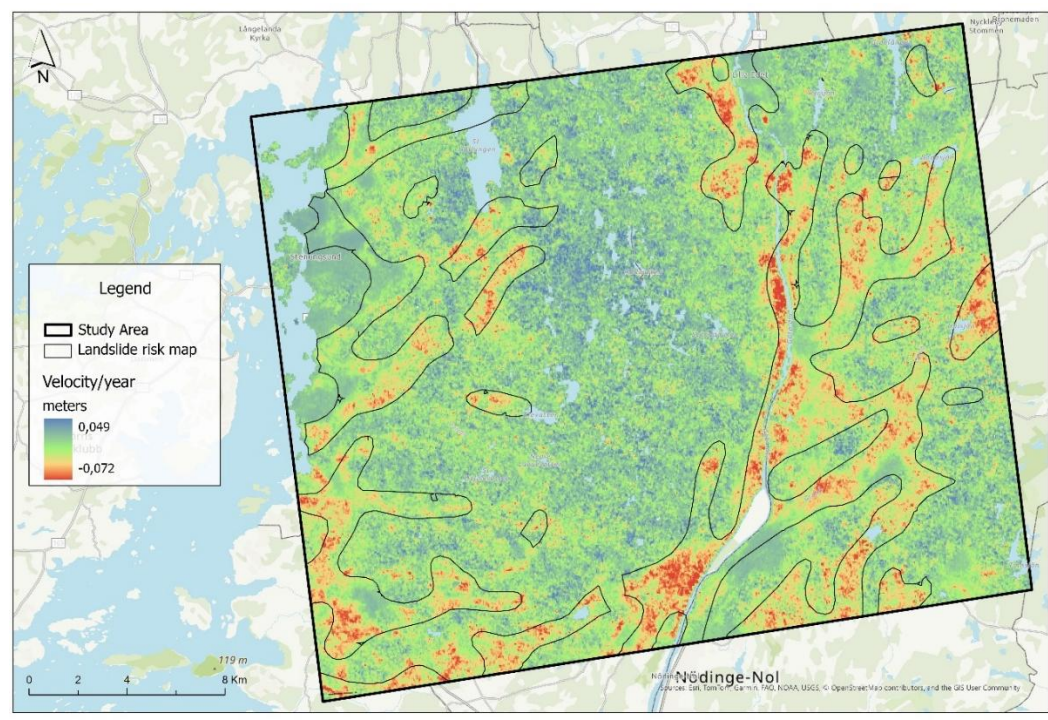


Figure 7. Velocity map from SBAS overlaid with the outline of the national landslide risk zones based on SGI risk mapping (2012a). The map displays annual displacement rates between 2017-2021. The velocity values range between +0,049 and -0,072 meters per year, with blue tones indicating uplift and red tones representing subsidence.

4.2.2 Göta River Valley Risk map

The landslide risk map for the Göta River valley from SGI was used to explore how well the SBAS ground motion results match the mapped risk levels. As shown in figure 8c, the map divides the area into five risk levels: low, medium, medium (secondary), high (secondary), and high. Areas with exposed bedrock are also included. The background was set to a grey basemap to improve visibility of the classified zones. The SBAS velocity map was clipped to match the classified risk layer (figure 8b), allowing for direct visual comparison between observed ground motion and mapped risk levels.

Most of the mapped risk zones are concentrated in the northern part of the study area (figure 8d), where the SBAS results generally show stable values or uplift. In contrast, the southern and central parts of the river valley (where the landslide risk is mainly classified as low) display a more varied pattern with both strong subsidence and uplift.

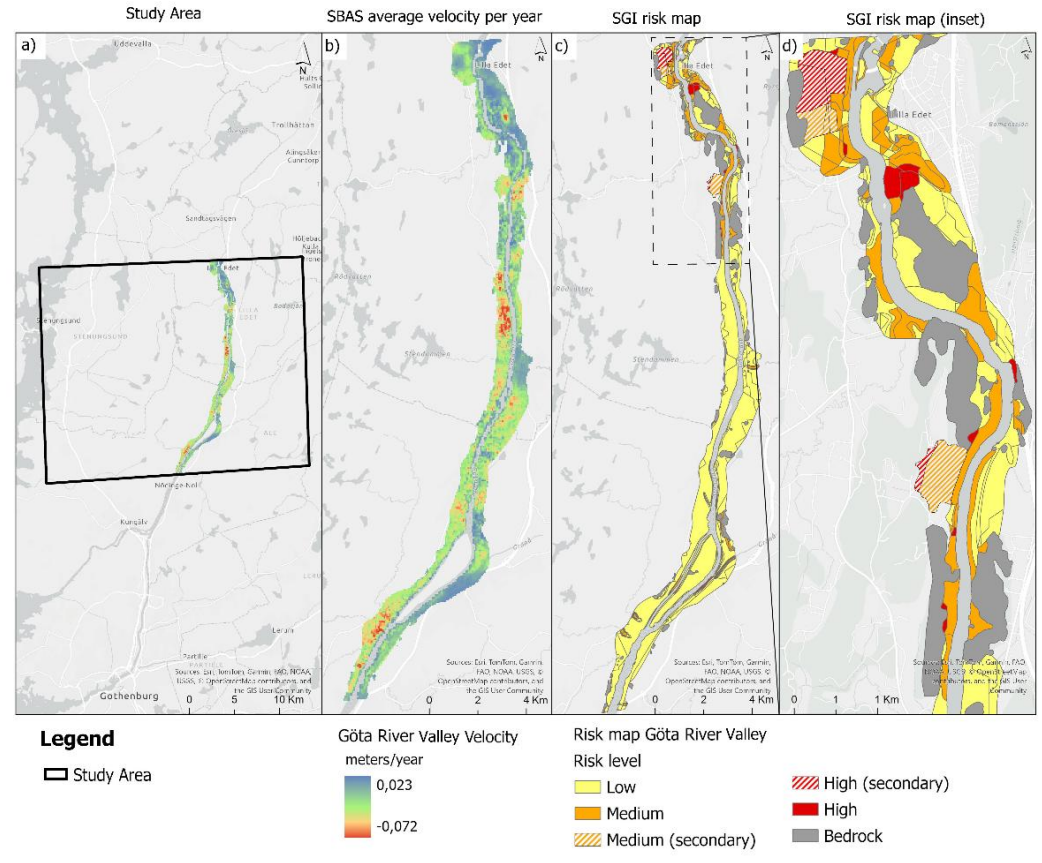


Figure 8. Comparison of ground deformation and landslide risk along the Göta River valley. a)Overview map showing the study area outlined in black. b) SBAS ground deformation rates in meters per year during the 2017-2021 study period c) Official landslide risk classification by SGI (2012a) for the same area, including low, medium, high, and secondary risk levels as well as bedrock exposure. d) Zoomed-in view of the northern portion of the risk map (dashed box in panel c), showing more detail of the high-risk zones.

Zonal statistics were used to calculate the average velocity for each risk level. The results show areas classified as "medium (secondary)" had the highest average subsidence within the study area with -0.024 m/year, followed by "low" risk areas at -0.019 m/year. Meanwhile, the "high" risk category had the smallest average subsidence at -0.002 m/year. These values are summarized in table 3 for each risk level. The majority of the mapped risk zones (including the areas with identified quick clay mapped as secondary risk) are located in the northern part of the study area. This is shown in the zoomed-in panel in figure 8d, which shows a cluster of medium, high and secondary risk polygons around Lilla Edet.

Table 3. Average SBAS velocity per year in meters during the study period for each Göta River landslide risk level within the study area. Negative values indicate subsidence.

Risk level	Mean Velocity (m/year)	
Low	-0.019	
Medium (secondary)	-0.024	
Medium	-0.012	
High (secondary)	-0.014	
High	-0.002	

4.3 Historical Landslides Analysis

Figure 9 shows the historical landslides in the study area, taken from SGI's national inventory. Each point was buffered by 100 meters to capture the average SBAS velocity around the landslide site. The points are color-coded by velocity in meters per year, with blue indicating uplift or stability and red indicating higher levels of subsidence.

Many of the landslides located along the Göta River valley overlap with areas showing ground motion during the study period. One example is a landslide from 2020, marked by the red square in the inset, which falls within the study period and shows relatively high rates of subsidence (around -0.020 to -0.029 m/year) surrounded by other known landslides which shows subsidence during the study period. Several other sites also show moderate movement, while others appear stable.

The dataset includes 87 mapped landslides, but only 19 have a known event date. Some of the undated events are dated to the 1800s or early 1900s. This makes it difficult to say whether movement observed in the SBAS data is related to the landslide or to ongoing processes in the same area.

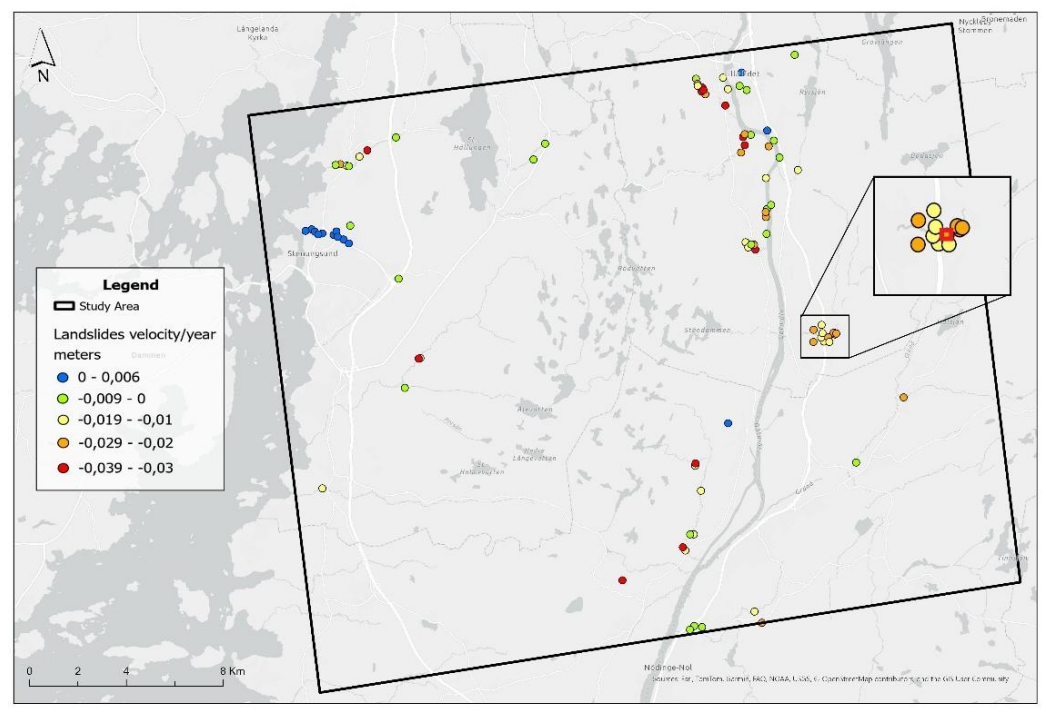


Figure 9. Historical landslide locations from SGI's inventory, each buffered by 100 metres and colour-coded by average SBAS velocity (m/year). Red and orange points indicate higher subsidence, while blue shows uplift or near-stable conditions. The inset highlights the only landslide in the dataset known to have occurred during the SBAS observation period (occurred in 2020).

4.4 Railway Deformation Analysis

To examine how ground motion might affect railway infrastructure, the average SBAS velocities were extracted along a 100-meter buffer around the railway network to include nearby terrain that might influence the stability of the tracks. The resulting map is shown in figure 10a, displaying deformation trends along the railway network during the study period. Red indicates subsidence and blue indicates uplift.

Several areas stand out in the velocity map, especially along the Göta River where multiple segments show relatively strong subsidence. The inset in figure 10a highlights these segments in more detail.

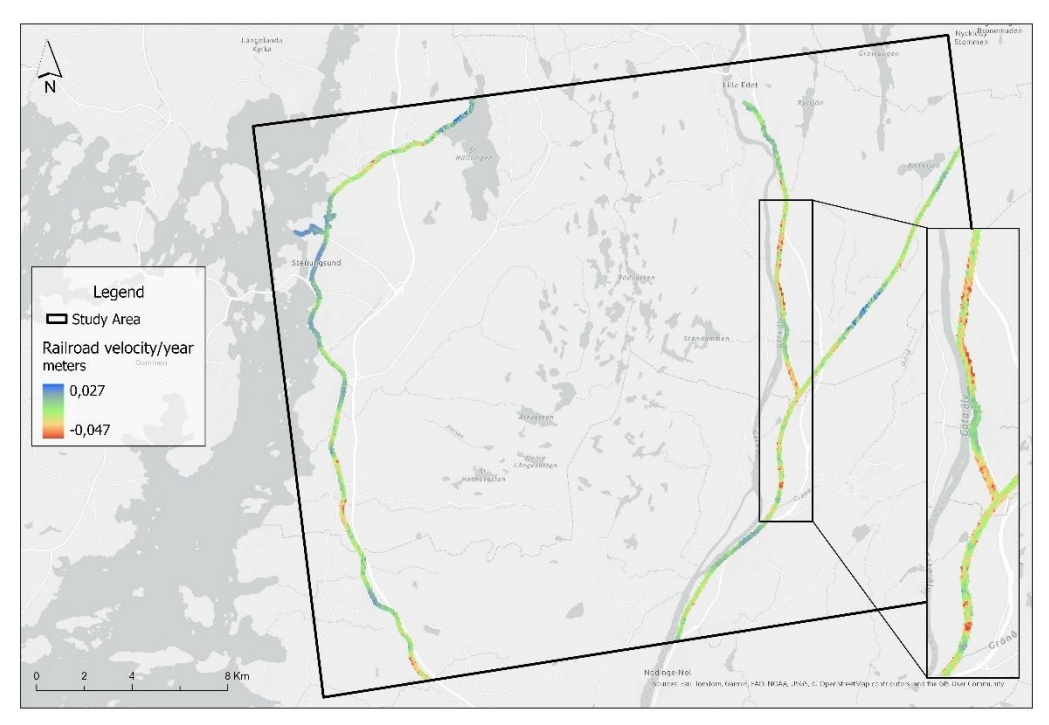


Figure 10a. SBAS average velocity map during the study period clipped to a 100-meter buffer around the railway lines. The values are displayed in meters per year, with blue indicating uplift, and red indicating subsidence. The inset shows the Göta River segment where stronger subsidence appears near the track

To simplify interpretation, the velocity data were grouped into four classes: low (> -0.002 m/year), moderate (-0.005 to -0.002 m/year), high (-0.010 to -0.005 m/year), and very high (< -0.010 m/year). These categories were used to classify the buffered railway segments by deformation level. Figure 10b shows these results, with red and orange sections marking areas where the underlying ground is subsiding more rapidly. The background was set to a grey basemap to improve visibility of the classified areas.

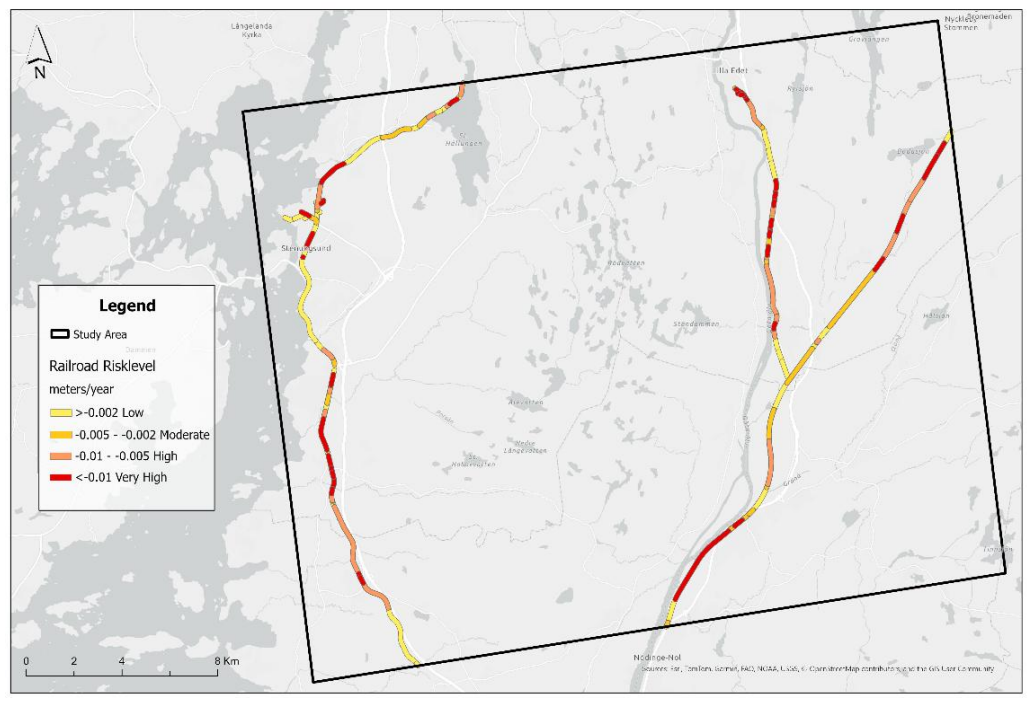


Figure 10b. Classified risk map for the railway network based on SBAS velocity thresholds within the study area outlined in black. Risk categories range from low (>-0.002 m/year) to very high (<-0.010 m/year), displayed with increasing subsidence from yellow to red.

4.5 Error Analysis

An evaluation of SBAS reliability was done by examining velocity uncertainty maps, spatial and temporal coherence, and coherence history for both ascending and descending datasets separately.

The velocity uncertainty maps (figures 11a and 11b) show the standard deviation of estimated linear velocities, with darker shades indicating greater uncertainty.

In the ascending dataset, the lowest uncertainties are found near the reference point and in areas with open terrain or infrastructure (figure 11a). Higher uncertainty is seen along the eastern and southern edges of the frame, particularly in forested regions, where signal decorrelation is more likely (Yunjun et al., 2019).

The descending dataset shows a slightly different pattern, with higher uncertainties along the outer margins of the frame (western and eastern edges) seen in figure 11b. Some central areas of the descending dataset maintain a relatively lower uncertainty.

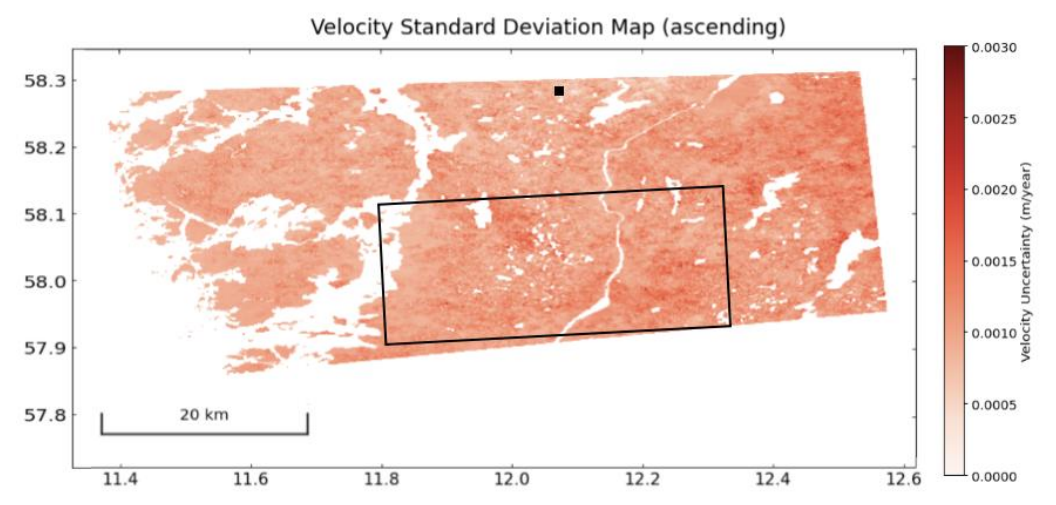


Figure 11a. Velocity uncertainty map for the ascending dataset, showing the standard deviation of the linear velocity estimates. Darker tones represent higher uncertainty. The study area is outlined in black. Lower uncertainties are seen near the reference point in the north and in open terrain. The image appears stretched due to display in geographic coordinates (WGS84).

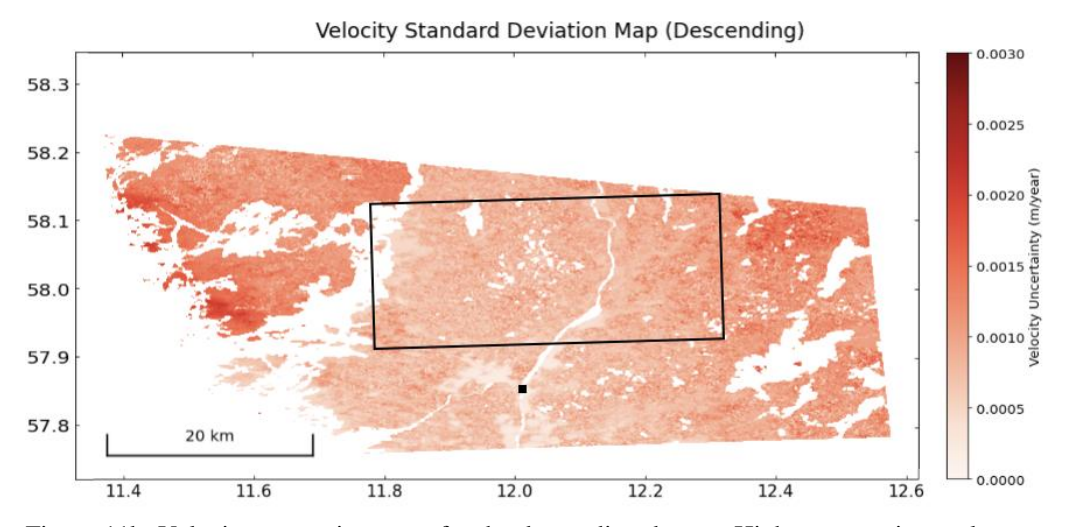


Figure 11b. Velocity uncertainty map for the descending dataset. Higher uncertainty values are concentrated along the outer edges of the scene and in forested areas. The central region generally displays more stable velocity estimates. The study area is outlined in black.

These spatial patterns align with zones of low spatial coherence in the Appendix (figures A4 and A5), confirming that areas of reduced coherence correspond to increased velocity uncertainty (Confuorto et al., 2017).

Temporal coherence maps (Appendix A, figures A6 and A7) illustrate phase stability over the observation period, with values ranging from 0 (unstable) to 1 (fully stable). Both tracks show high coherence along the Göta River valley, over lowlands, and in exposed bedrock or infrastructure zones, while forested areas, water bodies, and scene egdes show lower coherence.

Coherence history plots (figures 12a and 12b), show the minimum and maximum average spatial coherence values for each interferogram pair. Coherence values range from 0.30 to 0.85, but one ascending interferogram dips below 0.30 during a seasonal gap, and two descending interferograms also fall under 0.30 (see Appendix A, figures A2 and A3). To fill these gaps, custom image pairs were included, which increased both the temporal baselines (up to 132 days for ascending, 204 days for descending) and the

perpendicular baselines (up to 228 m for ascending) beyond the usual SBAS limits of 6 days and 200 m. Despite this, all interferograms were kept in the analysis.

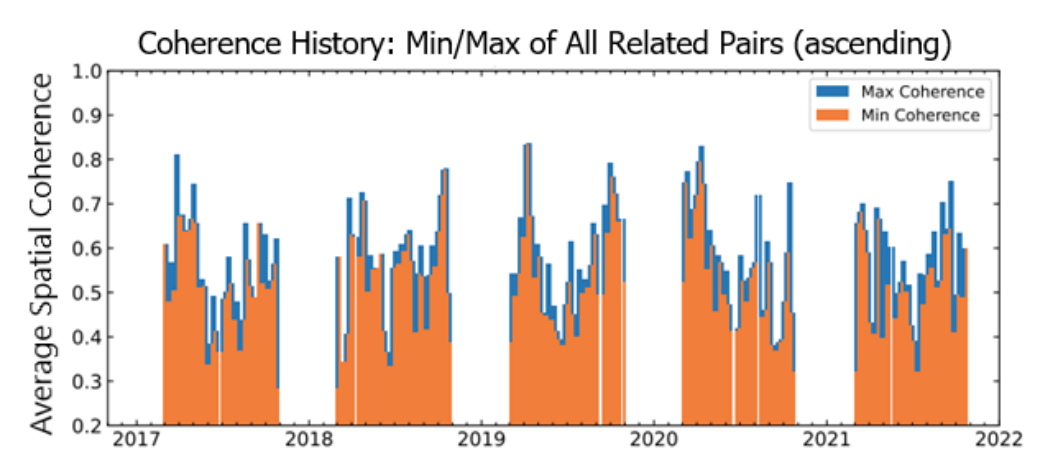


Figure 12a. Coherence history of all interferometric pairs in the ascending dataset, showing the minimum (orange) and maximum (blue) average spatial coherence values over time. Coherence remained mostly above the commonly used threshold of 0.3 (Yunjun et al., 2019), except for one pair during a seasonal gap.

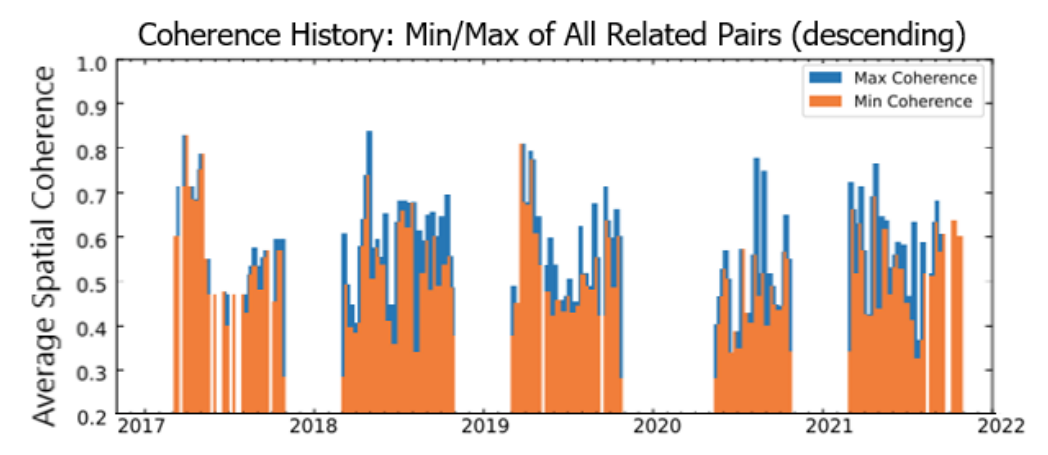


Figure 12b. Coherence history of all interferometric pairs in the descending dataset, displaying minimum (orange) and maximum (blue) average spatial coherence. While more variability is seen compared to the ascending dataset, especially at start and end of the time series (including two interferograms below 0.30) all interferograms were included in SBAS processing (Yunjun et al., 2019).

4.6 GNSS Validation

To assess consistency between satellite and ground-based observations, SBAS LOS time series from both ascending and descending tracks were compared with vertical GNSS displacements at the 0LED station. This station lies within the study area and provides continuous vertical motion data over the same 2017–2021 period.

Figure 13 plots the SBAS LOS displacement (ascending in blue, descending in orange) alongside the GNSS vertical trend in purple. All plots have been resampled to monthly values for clarity, with values referenced to the first common acquisition in March 2017. Straight lines connect seasonal gaps in the SBAS stacks.

The ascending LOS series shows a clear uplift signal between mid-2018 and early 2019, before gradually declining back toward zero by 2021. In contrast, the descending LOS series show steady subsidence from 2018 onward, with a sharp drop after the 2020

seasonal gap. The GNSS vertical measurements follows a much gentler uplift over the entire period.

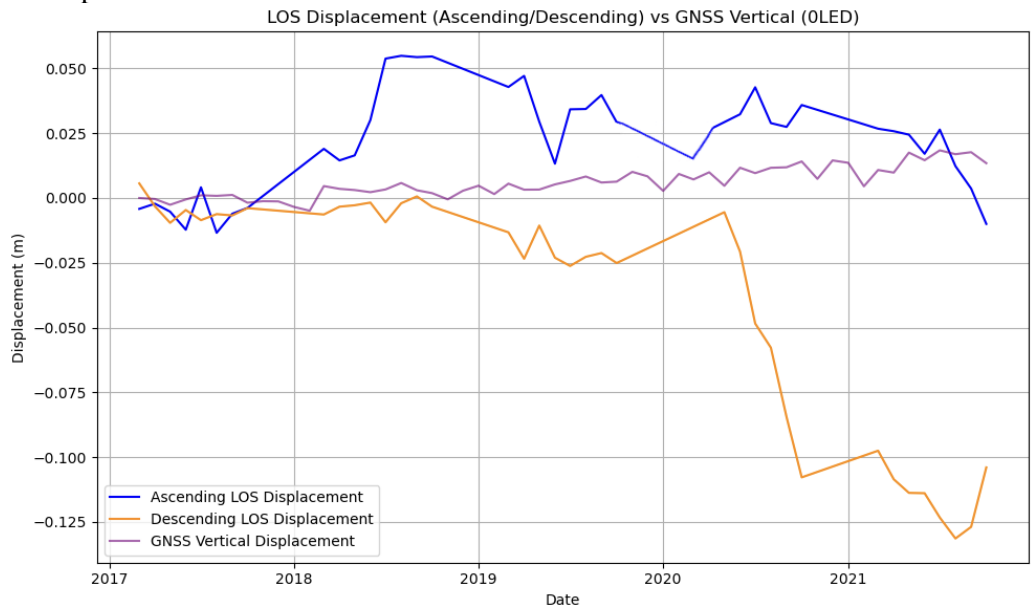


Figure 13. LOS displacement time series derived from SBAS-InSAR for both ascending (blue) and descending (orange) tracks compared to vertical displacement from vertical GNSS measurements at the 0LED station (purple). Displacement values are referenced to the first available acquisition (March 2017), and resampled to monthly values. Temporal gaps in the SBAS acquisitions appear as linear connections between available points. The figure illustrates the consistency between satellite-derived and ground-based measurements over the 2017–2021 observation period.

5 Discussion

5.1 Main Findings

5.1.1 Ground Deformation Patterns

The SBAS results show a spatial difference in ground motion across the study area during March 2017- November 2021 (figure 5). Most of the subsidence is found in low-lying parts, especially along the Göta River valley and in areas mapped as containing postglacial fine sediments and other soft soils. These areas often show subsidence in the velocity and displacement map, indicating downward movement of up to -0.072 m/year Meanwhile, areas at higher elevation in the northern and central regions, tend to be more stable or even show slight uplift (Zhang, J. et al., 2022).

These patterns align well with geological and topographical factors. The slope and soil zonal statistics show that the highest subsidence rates occur in flatter areas with clay, silt, or sand deposits (see Appendix B, table B1, figure B1 and B2). This is likely not due to slope failure, but rather due to gradual settlement processes in compressible soils. Such materials are more sensitive to compaction, moisture changes, or loading effects (from infrastructure or groundwater changes), leading to slow vertical motion rather than slope-driven landslides (Galloway & Leake, 2017). In contrast, steeper slopes with exposed bedrock (although theoretically more prone to landslides due to gravitational forces) may appear more stable in the SBAS results. These slopes may still be at risk for

landslides or debris fall, but such events are often rapid, making them less detectable in long term velocity maps (Intrieri et al., 2018; Li et al., 2022).

Faster ground movement can sometimes be identified in individual time series, especially in areas with high coherence. However, rapid slope failures often result in a loss of coherence, which makes them harder to detect using SBAS alone (Li et al., 2022). In such cases, other data sources like GNSS measurements or aerial imagery are often needed for confirmation (Intrieri et al., 2018). Similar results have been noted by Zhang, J. et al. (2022) who found that SBAS-InSAR reliably showed slow deformation in low-gradient, fine-sediment terrains while underestimating rapid mass movements on steep slopes.

5.1.2 Susceptibility and Risk maps

Comparison of SBAS average velocity with SGUs national landslide susceptibility map reveals generally good agreement. Areas classified as "significant susceptibility to landslides" show the largest average subsidence, confirming that mapped high-risk zones correspond to active ground motion during 2017–2021. A small number of unmapped areas also showed notable subsidence, suggesting InSAR can detect instabilities overlooked by earlier assessments (Ciampalini et al., 2016).

Around Stenungsund, high susceptibility is likely mapped due to presence of post-glacial clays and past landslides, yet SBAS results show slight uplift. Since both ascending and descending stacks have high coherence here, those uplift values are likely reliable and might be due to recent development. However, most high-risk areas do show subsidence, reinforcing that SGUs susceptibility mapping aligns well with the SBAS results.

It should be noted that a distinct pattern of "noticeable susceptibility" polygons is shown on the national susceptibility map. These were retained in the analysis but may introduce some error. Low susceptibility areas occupy 0.12% of the mapped zones and noticeable susceptibility covers only 0.06% so the analysis therefore focuses on high susceptibility classes. The different susceptibility classes mapped in the study area is shown in Appendix B (figure B3).

When the Göta River valley risk map is examined, the secondary-risk polygons, both medium and high, reveal an interesting pattern. These areas were mapped based on the presence of quick clay and the potential for retrogressive landslides if disturbed. During 2017–2021, the medium (secondary) risk polygons showed the greatest average subsidence, followed by the low-risk zones, while the high-risk polygons showed the least movement. One explanation is that the high-risk areas were defined through detailed soil composition, groundwater and slope-stability studies (SGI, 2012a), so they may contain sensitive materials that have not yet been destabilized. In contrast, some medium (secondary) mapped zones between 2009 and 2011 may have become destabilized in the years since the mapping, giving the higher subsidence observed by SBAS. A similar trend was reported by Zhang J. et al. (2022), who found SBAS being able to detect evolving instability in previously mapped risk zones.

This could also be explained by the difference in scale. SBAS resolution of about 80 m will average out small, localized motion, whereas geotechnical investigations works at a much finer scale. As a result, SBAS with this resolution is better suited for regional-scale screening and might detect areas where older susceptibility assessments might need updating. For site-specific evaluation (especially in high-risk or complex terrain) in-situ methods such as borehole drilling, GNSS measurements and detailed slope stability assessments are still needed.

5.1.3 Historical landslides

Several mapped historical landslides in the study area show subsidence in the SBAS results, particularly along the Göta River valley. Most of the landslides lack dates and some date back to the 1800s and early 1900s, and in many of those locations the 2017–2021 SBAS record shows little to no movement, suggesting those slopes have since stabilized

In some cases, mapped landslides do not correspond with any obvious displacement in the SBAS results. This may reflect stability but could also be due to InSAR limitations with low coherence over dense forest, steep slopes or water surfaces or due to gaps in the landslide inventory.

One landslide that occurred during the SBAS observation period does show subsidence in both ascending and descending tracks, along with a cluster of past landslides showing similar patterns, demonstrating SBASs ability to capture reactivated slope movement.

In Stenungsund, several mapped landslides along a narrow stream instead show slight uplift in the SBAS results. Coherence here remains high, but the descending data show greater uncertainty, likely a consequence of viewing geometry, distance from the reference point and mixed land cover. Without precise dates for these events, uplift may reflect construction or drainage changes rather than slope stability.

This comparison suggests that SBAS-InSAR can help identify both ongoing and reactivated landslides, but its reliability depends on coherence, spatial resolution and the quality of the landslide inventory. In areas where movement was not detected, it could be due to either stability or limitations in the method. Combining InSAR with field observations and an updated landslide inventory will improve identification of slopes needing additional monitoring.

5.1.4 Railways

The SBAS velocity data showed that most of the railway segments in the study area appeared stable, but some areas (particularly near the Göta River valley) showed signs of subsidence. A 100-meter buffer was applied around the railway lines to extract nearby velocity values and identify segments with higher displacement.

Some of the observed movement could be related to soft soils, erosion near the river, or loading from infrastructure, although these causes were not investigated in detail. The goal was to flag areas for potential investigations.

This study used C-band with about 80 m resolution and results were classified with custom thresholds rather than standardized criteria. In some cases these classes didn't match the mean velocities because the 100 m buffers likely mixed stable and unstable pixels, and the coarse pixel size smooths out narrow features like railway tracks. Li et al. (2022) similarly note that SBAS at this resolution can underestimate linear infrastructure deformations unless paired with higher-resolution data.

Also, by averaging the ascending and descending LOS datasets, only vertical displacement was analyzed. This means possible horizontal motion was not captured which is another important factor for railway safety (Li et al., 2022). A more detailed decomposition or comparison with GNSS data would be beneficial in these areas (Del Soldato et al., 2021).

Despite the limitations, the results help identify locations where monitoring could be useful, especially if used together with other data sources.

5.1.5 Error Analysis

The quality of the SBAS results was assessed using a combination of velocity uncertainty maps (figure 11a and 11b), coherence history plots (figure 12a and 12b), spatial coherence maps (Appendix A, Figures A4 and A5), and temporal coherence maps (Appendix A, figures A6 and A7). While the coherence maps were not shown in the main results, they were reviewed during the analysis and supported the reliability patterns seen in the uncertainty maps.

Uncertainty in the velocity estimates grows the farther the pixel is from the reference point for both stacks. In the ascending stack (197 interferograms), the smallest uncertainties are around its reference pixel in the north and over open terrain (Figure 11a), while values increase toward the eastern and southern edges of the study area. In the descending stack (166 interferograms), uncertainty is lowest near its own reference pixel and higher along the western and eastern edges (Figure 11b). This pattern reflects that velocities are calculated relative to the chosen reference pixel (Berardino, 2002; Yunjun et al., 2019).

The spatial coherence maps (Appendix A, Figures A4 and A5) show that open terrain and urban areas, especially along the Göta River valley, maintain higher coherence over time. In contrast, forested or topographically complex zones had weaker coherence and greater velocity uncertainty. Other SBAS studies have similarly linked low coherence with higher uncertainty (Confuorto et al., 2017).

Temporal coherence maps (Appendix A, Figures A6 and A7) show that most of the study area retains stable phase behavior over time. Some reductions in coherence occur in the middle of the descending track, coinciding with areas of mixed vegetation and land cover that weaken the radar signal (Li et al., 2022).

The coherence history plots provided a summary of average coherence across all interferograms. Most interferograms exceeded the commonly used threshold of 0.3 for SBAS-InSAR time-series analysis (Ferretti et al., 2001; Yunjun et al., 2019). A few interferograms dropped below the 0.3 threshold, mostly due to seasonal gaps or image pairs that did not meet the standard SBAS criteria. To keep the time-series as complete as possible, some additional pairs were included due to seasonal gaps but also lack of available scenes, even though they slightly exceeded the baseline limits. Using custom pairs to fill seasonal gaps has been applied in other SBAS workflows to maintain network connectivity (Li et al., 2022).

Overall, the results from the uncertainty maps, coherence plots, and time series quality checks suggest that the SBAS data can be considered reliable across much of the study area. Areas with lower coherence, long data gaps, or that are far from the reference points should be interpreted more carefully. These checks were useful for understanding where the displacement data is most trustworthy.

5.1.6 GNSS Validation

The SBAS LOS displacement was compared with GNSS vertical displacement at the 0LED station within the study area. The ascending SBAS LOS stack follows the GNSS vertical trend slightly, both showing slight uplift from 2017–2021, indicating reliable coherence and geometry for the ascending orbit at this pixel. The descending SBAS series had a noticeable drop after 2020, showing a downward shift not seen in the GNSS record.

Part of this discrepancy may come from viewing geometry or lower temporal coherence in the descending stack (Appendix A, figures A6 and A7) and a longer seasonal data gap. Vegetation and mixed land cover at the station also increase radar speckle which is random phase noise caused by multiple scatterers within a pixel (ESA, 2007).

Differences in the number of image pairs (197 vs. 166 interferograms), reference-point placement, and the fact that SBAS measures LOS displacement (while GNSS records true vertical motion) makes the comparison only approximate (Ferretti et al., 2001; Crosetto et al., 2008). A similar inconsistency between LOS and vertical GNSS trends was noted by Armaş et al. (2016) in urban settings. Also, validation at a single station/pixel cannot capture accuracy across the study area. Additional GNSS stations or ground based observations would strengthen the reliability in SBAS results (Fabris et al., 2022; Nikolakopoulos et al., 2023).

5.2 Method - Reflections and Limitations

This study relied on SBAS-InSAR processing of Sentinel-1 C-band data using HyP3 and MintPy, followed by statistical and spatial analysis in ArcGIS Pro. The methodology had several strengths in terms of accessibility, processing efficiency, and suitability for large-scale ground deformation monitoring. However, some limitations were also noted in the processing steps and interpretation of results.

5.2.1 InSAR processing and workflow

The initial interferometric processing was performed using the ASF HyP3 platform. HyP3 automates core processing steps and enables batch handling of Sentinel-1 scenes, which significantly reduced the workload and made it easier to test different coverage options. This user-friendly and time-efficient setup was particularly valuable during the early stages of the project. According to Yi et al. (2023), cloud-based platforms like this can reduce processing times from weeks to just a few hours.

However, HyP3 also has limitations. It is currently only offering products from Sentinel-1 C-band which limits the applications of the analysis. It does not offer adjustments to certain parameters such as filtering strength, unwrapping algorithms, or coherence thresholds. And because the highest resolution for multilooking of 10×2 yields an 80 m ground-range resolution (with 40 m between pixel centers), it cannot resolve displacement signals on scales smaller than roughly 80 m, making it difficult to pick up narrow or subtle features such as rail tracks (Yi et al., 2023).

SBAS processing was completed using MintPy, which includes all key steps: DEM error correction, tropospheric delay correction, network inversion, and generation of velocity and displacement maps. A significant challenge was selecting an optimal Sentinel-1 frame where the study area was centered, covered by both orbit directions, and offered sufficient coherence. Frame selection had a clear impact on the final coherence and quality of the time series. Reference-pixel choice in MintPy also influences the spatial distribution of uncertainty. Pixels chosen by default may not lie in the most stable zones for the specific terrain of the study (Yunjun et al., 2019).

An important issue was the automatic water masking applied during MintPy processing. One GNSS station on a river island was excluded due to being masked as water in the waterMask.h5 file. This water mask is automatically generated by ASF using data from OpenStreetMap and/or ESA WorldCover, depending on geographic location (Alaska Satellite Facility, n.d.-a). This prevented the use of an otherwise valuable GNSS station. Better control of the water mask or manual editing could address this in future work.

After applying a 10×2 look in HyP3, the Sentinel-1 C-band SBAS products have an effective ground resolution of 80 m with a 40 m pixel spacing. Once reprojected to SWEREF 99 TM they are resampled to a 45×45 m pixel grid. While appropriate for regional studies, this resolution may not be sufficient for small-scale or infrastructure-

focused analysis. For detailed studies, other radar wavelengths such as L-band or X-band could be beneficial in vegetated or urban areas.

5.2.2 Temporal and Seasonal Gaps

Another issue was a longer gap in the descending time series between October 2019 and May 2020 (seasonal gap was set between November-March). Although Sentinel-1 scenes were available, they did not meet the SBAS baseline conditions, so no interferograms were created for that period. This led to a longer gap in the time series and likely contributed to the displacement anomalies seen in the descending results during that time. More careful pair selection or custom pairs might have helped fill this gap.

Seasonal gaps were also used by excluding acquisitions from November to March to avoid decorrelation from snow cover. While this strategy helped maintain higher coherence during winter months (Li et al., 2022), it also reduced the number of usable scenes each year. The time series became more stable but less continuous. A more detailed seasonal investigation (such as interpreting aerial imagery) could have increased data quality. While the observation period (March 2017 to November 2021) was long enough for velocity trend analysis, consistent acquisitions across all seasons would improve the quality of future analysis.

Using the same reference date for both ascending and descending stacks would likely reduce minor offsets when comparing cumulative displacements between the two geometries. In this study, the reference dates differed by one week, which had likely had little impact on long-term velocity estimates but could introduce small biases in absolute displacement.

5.2.3 Interpreting Velocity vs. Displacement

Both velocity and cumulative displacement maps were generated, but velocity was used as the main dataset for analysis. Velocity maps are more stable over time and less sensitive to the reference date, making them better suited for identifying long-term deformation patterns (Ren et al., 2022; Yunjun et al., 2019). They are also easier to interpret when comparing different areas or performing zonal statistics.

Cumulative displacement maps are more sensitive to noise, but are useful for tracking deformation over time, especially in cases where movement may be accelerating or seasonal by looking at individual scenes from the time series (Intrieri et al., 2018; Confuorto et al., 2017). In this study, cumulative displacement maps and individual timeseries scenes were mainly used for understanding the extent of deformation, while velocity maps were used for quantitative analysis. Cumulative displacement may still be more informative in future site-specific studies, particularly if supported by external data sources like GNSS or rainfall records (Dong et al., 2023).

5.2.4 Averaging of Ascending and Descending Orbits

In this study, the ascending and descending velocity maps were averaged to create a single layer. This helped reduce some geometric distortions and provided a more continuous picture of ground motion across the study area.

However, averaging has clear limitations when it comes to interpreting the direction of movement. SAR satellites are side-looking and since the two orbits view the surface from opposite sides, combining them without other processing tends to cancel out motion that occurs in the east—west direction (north-south motion is difficult to assess as SAR satellites cannot detect motion along its flight path (Hanssen, 2001)). Vertical

movement remains in the averaged result, but it can be underestimated depending on the slope direction and how much horizontal motion is present (Li et al., 2022).

5.3 Possible Improvements and Future Studies

5.3.1 Separating Vertical and Horizontal Components

In this thesis, ascending and descending LOS velocities were averaged to give a single, velocity map. While this still allowed for interpretation of broad deformation patterns, it cancels out most east—west motion (Hanssen, 2001). Future work should apply geometric decomposition of the ascending and descending LOS stacks using incidence and azimuth angles to decompose vertical and east—west displacements for a more accurate result (Guzzetti et al., 2009; Lazecky et al., 2016).

5.3.2 Sensor Selection and Resolution

Sentinel-1 C-band data provided sufficient revisit times but limited spatial resolution (80 m). For narrower targets such as railway lines or small landslides, higher-resolution X-band (TerraSAR-X) can detect more detailed deformation features (Krieger et al., 2007). Rao & Tang (2014) demonstrated that applying SBAS-InSAR to X-band data along a high-speed railway enabled detection of movements along the tracks, showing the benefit of matching sensor resolution to target features and analysis scale. In vegetated or forested zones, L-band sensors (ALOS-2) offer deeper penetration and better coherence (JAXA, n.d.). For example, SLUs remote-sensing research on forestry shows that L-band remains coherent through dense canopy and is used for mapping forest inventories (SLU, 2024). Combining SAR bands (C + X or C + L) will likely improve coverage and detection in complex terrain (Lu et al., 2007). Commercial constellations like ICEYE, with up to 25 cm resolution and hourly revisits, could support near-real-time monitoring of critical areas (Ignatenko et al., 2022). This demonstrates how sensor capabilities are improving, even though these high-resolution datasets currently aren't freely accessible.

5.3.3 Integrating InSAR with Susceptibility Mapping and Machine Learning

SBAS-InSAR highlights areas of active subsidence that may have been missed in susceptibility maps. For example, Ciampalini et al. (2016) used PS-InSAR velocities with a Random Forest model to correct errors and detect unmapped slow-moving slopes in an existing landslide map. Kulsoom et al. (2023) paired SBAS-InSAR velocity rates with several machine-learning models to create a new susceptibility map, making it more reliable than either method alone.

Future work could similarly use velocity time series with machine-learning models to adjust susceptibility levels in near real time. Also, integrating these deformation results with geospatial layers such as slope angle, soil type, and rainfall intensity (Ardizzone et al., 2009; Dai et al., 2002) would allow predictive models to detect where susceptibility classifications may have changed since the last inventory, to guide prioritized field investigations.

5.3.4 Lessons from Norway's National Monitoring

Norway's landslide monitoring program shows how SBAS-InSAR can be used to monitor landslides. Their national NIFS project (Naturfare, Infrastruktur, Flom og Skred) brings together government agencies and applies SBAS-InSAR across large regions to flag areas of increasing risk (NVE, 2015). Sentinel-1 is used for regional monitoring with the addition of X-band sensors such as TerraSAR-X/TanDEM-X or Cosmo-Skymed for prioritized areas needing higher resolution monitoring (NVE, 2015).

At higher-risk sites (such as the Gjerdrum quick-clay landslide after 2020) Norwegian authorities installed permanent ground-based InSAR sensors to track scarp movement in near real time, successfully detecting renewed creep hours before new slope failures occurred (NVE, 2024). Ground-based InSAR systems continuously scan fixed zones and deliver detailed deformation updates, overcoming limitations of satellite revisit times and resolution.

A similar setup in Sweden in clay-rich areas such as the Göta River valley, would deliver continuous, all-weather deformation updates that could complement SBAS screening and help catch early warning signs at high-risk infrastructure sites.

By combining these improvements: decomposing vertical and horizontal SBAS motion and using finer-resolution sensors where needed to efficiently integrate deformation into susceptibility models which is supported by ground-based InSAR installations at risk areas, landslide mapping and monitoring can evolve from regional screening to a dynamic, multi-scale system capable of early warning and targeted risk management.

6 Conclusion

This study examined how SBAS-InSAR time series analysis can be used to detect and monitor ground deformation in landslide-prone areas, such as Västra Götaland as a case study. The resulting velocity deformation maps show that SBAS is a useful method for observing long-term motion, especially subsidence in low-lying areas and along critical infrastructure such as railways. The method showed how deformation varies across the region and was able to detect movement in areas both inside and outside known risk zones.

Several limitations became clear during this study. Coherence values were reduced in forested areas, which affected the reliability of the results in those locations. The spatial resolution of 80 meters also made it difficult to detect small-scale ground motion that might have been averaged out. Finally, because ascending and descending observations were averaged rather than decomposed, horizontal (east—west) movement could not be separated from the vertical motion.

Even with these limitations, the results show that SBAS-InSAR can be a useful tool to support current methods used for landslide risk mapping. It allows tracking of ground motion over time, which can reveal slow-moving deformation and help detect early signs of instability. This could help authorities and planners to follow up with more detailed investigations or monitoring, especially around vulnerable infrastructure. While it cannot replace detailed geotechnical surveys, SBAS offers cost-effective, region-scale monitoring that supports early warning of potential risk zones. By combining SAR-data of different wavelengths with additional datasets such as rainfall and hydrological records, geological and soil maps, or GNSS observations, the reliability of the deformation can be improved, supporting more accurate and proactive landslide risk assessments.

Acknowledgement

I would like to thank my supervisor Ian Brown at Stockholm University for his guidance throughout this project. His straightforward feedback and support was especially helpful during the technical steps of the project and interpreting the results.

Thanks also to Sofia Åsberg at Trafikverket, whose encouragement and practical input were a great support during the entire thesis period. Her help in connecting me with professionals in the field was much appreciated.

Finally, I want to thank my friend and study colleague Filippa Törnkvist for her moral support throughout this work.

References

Abdelfattah, R. (2023). Land subsidence and surface water extent relationship assessment using Sentinel-1 & 2 data in the Cap-Bon Peninsula in Tunisia. In *IGARSS* 2023 – 2023 IEEE International Geoscience and Remote Sensing Symposium (pp. 2866–2869). https://doi.org/10.1109/IGARSS52108.2023.10283317

Ado, M., Amitab, K., Maji, A. K., Jasińska, E., Gono, R., Leonowicz, Z., & Jasiński, M. (2022). Landslide susceptibility mapping using machine learning: A literature survey. *Remote Sensing*, 14(14), 3029. https://doi.org/10.3390/rs14133029

Afeni, T. B., & Cawood, F. (2013). Slope monitoring using total station: What are the challenges and how should these be mitigated? *South African Journal of Geomatics*, 2, 41–53.

Alaska Satellite Facility. (n.d.-a). *Sentinel-1 InSAR product guide*. Retrieved April 10, 2025, from https://hyp3-docs.asf.alaska.edu/guides/insar-product-guide/

Alaska Satellite Facility. (n.d.-b). *OpenSARLab*. Retrieved April 10, 2025, from https://asf.alaska.edu/asf-services-opensarlab/

Alén, C., Bengtsson, P.-E., Berggren, B., Johansson, L., & Johansson, Å. (2000). Skredriskanalys i Göta älvdalen – Metodbeskrivning (Report No. 58). Statens Geotekniska Institut. Retrieved March 7, 2025, from https://www.swedgeo.se

Andersson, M., Åberg, A., Carlsson, J., Svalgård Jarcem, S., Waidringer, J., Nelander, L., & Vuorenmaa Berdica, K. (2023). *Samhällsekonomiska effekter av jordskredet vid E6 Stenungsund* (Uppdragsnummer 10361637) [Report]. WSP Advisory. Retrieved March 15, 2025, from https://wsp.com

Andersson-Sköld, Y., Torrance, J. K., Lind, B., Odén, K., Stevens, R. L., & Rankka, K. (2005). Quick clay—A case study of chemical perspective in Southwest Sweden. *Engineering Geology*, 82(3–4), 195–212. https://doi.org/10.1016/j.enggeo.2005.09.014

Ardizzone, F., Rossi, M., Calò, F., Paglia, L., Manunta, M., Mondini, A. C., Zenia, G., Reichenbach, P., Lanari, R., & Guzzetti, F. (2009). Preliminary analysis of a correlation between ground deformations and rainfall: The Ivancich landslide, central Italy. *Remote Sensing of Environment*, 113(8), 1661–1674. https://doi.org/10.1016/j.rse.2009.02.004

Armaş, I., Gheorghe, M., Lendvai, A. M., Dumitru, P. D., Bădescu, O., & Călin, A. (2016). InSAR validation based on GNSS measurements in Bucharest. *International Journal of Remote Sensing*, 37(23), 5565–5580. https://doi.org/10.1080/01431161.2016.1244367

ASF OpenSARLab. (2024). opensarlab_MintPy_Recipe_Book (Jupyter notebooks). GitHub. Retrieved February 5, 2025, from https://github.com/ASFOpenSARlab/opensarlab_MintPy_Recipe_Book

Azarafza, M., Azarafza, M., Akgün, H., Atkinson, P. M., & Derakhshani, R. (2021). Deep learning-based landslide susceptibility mapping. *Scientific Reports*, 11, 24112. https://doi.org/10.1038/s41598-021-03585-1

- Barra, A., Monserrat, O., Mazzanti, P., Esposito, C., Crosetto, M., Mugnozza, G.S., (2016). First insights on the potential of Sentinel-1 for landslides detection. *Geometics, Natural Hazards and Risk* 7, 1874–1883. https://doi.org/10.1080/19475705.2016.1171258
- Berardino, P., Fornaro, G., Lanari, R., & Sansosti, E. (2002). A new algorithm for surface deformation monitoring based on small baseline differential SAR interferograms. *IEEE Transactions on Geoscience and Remote Sensing*, 40(11), 2375–2383. https://doi.org/10.1109/TGRS.2002.803792
- Ciampalini, A., Raspini, F., Lagomarsino, D., Catani, F., & Casagli, N. (2016). Landslide susceptibility map refinement using PSInSAR data. *Remote Sensing of Environment*, 184, 302–315. https://doi.org/10.1016/j.rse.2016.07.018
- Confuorto, P., Di Martire, D., Centolanza, G., Iglesias, R., Mallorqui, J.J., Novellino, A., Plank, S., Ramondini, M., Thuro, K., & Calcaterra, D. (2017). Post-failure evolution analysis of a rainfall-triggered landslide by multi-temporal interferometry SAR approaches integrated with geotechnical analysis. *Remote Sensing of Environment*, 186, 195-205. https://doi.org/10.1016/j.rse.2016.11.002
- Conoscenti, C., Rotigliano, E., Cama, M., Caraballo-Arias, N. A., Lombardo, L., & Agnesi, V. (2016). Exploring the effect of absence selection on landslide susceptibility models: a case study in Sicily, Italy. *Geomorphology*, 261, 222-235. https://doi.org/10.1016/j.geomorph.2016.03.006
- Crosetto, M., Monserrat, O., Cuevas-González, M., Crippa, B., & Devanthéry, N. (2016). Persistent Scatterer Interferometry: A review. *ISPRS Journal of Photogrammetry and Remote Sensing*, 115, 78–89. https://doi.org/10.1016/j.isprsjprs.2015.10.011
- Cruden, D & Varnes, D.J. (1996). Landslide Types and Processes. In: Turner, A.K., Schuster, R.L. (Eds.). *Landslide Types and Processes*. Transportation Research Board, U.S. National Academy of Sciences, Special Report, 247: 36-75. Special Report National Research Council, Transportation Research Board. 247. 36-57.
- Dabiri, Z. & Nilfouroushan, F. (2024) Enhancing Landslide Preparedness: Leveraging EGMS Products and SBAS-InSAR for Pre-Event Ground Deformation Monitoring along the E6 Highway near Stenungsund in Southern Sweden. EGU *General Assembly 2024, Vienna, Austria, 14–19 Apr 2024* (EGU24-12802). https://doi.org/10.5194/egusphere-egu24-12802
- Dai, F. C., Lee, C. F., & Ngai, Y. Y. (2002). Landslide risk assessment and management: an overview. *Engineering Geology*, 64(1), 65–87. https://doi.org/10.1016/S0013-7952(01)00093-X
- Dee, D. P., Uppala, S. M., Simmons, A. J., Berrisford, P., Poli, P., Kobayashi, S. ... & Vitart, F. (2011). The ERA-Interim reanalysis: Configuration and performance of the data assimilation system. *Quarterly Journal of the Royal Meteorological Society*, 137(656), 553–597. https://doi.org/10.1002/qj.828
- Del Soldato, M., Confuorto, P., Bianchini, S., Sbarra, P., Casagli, N. (2921) Review of Works Combining GNSS and InSAR in Europe. *Remote Sensing*, 13(9), Article 1684. https://doi.org/10.3390/rs13091684

Dong, J. H., Niu, R. Q., Li, B. Q., Xu, H., & Wang, S. Y. (2023). Potential landslides identification based on temporal and spatial filtering of SBAS-InSAR results. *Natural Hazards and Earth System Sciences*, 14(1), 52–75. https://doi.org/10.1080/19475705.2022.2154574

EO Portal. (n.d.-a). *Copernicus Sentinel-1*. European Space Agency. Retrieved April 2, 2025, from https://www.eoportal.org/satellite-missions/copernicus-sentinel-1#eop-quick-facts-section

EO Portal. (n.d.-b). *TerraSAR-X – Mission capabilities*. Retrieved May 18, 2025, from https://www.eoportal.org/satellite-missions/terrasar-x#mission-capabilities

EO Portal. (n.d.-c). *ALOS-2 – Mission capabilities*. Retrieved May 18, 2025, from https://www.eoportal.org/satellite-missions/alos-2#mission-capabilities

Erener, A., Sivas, A. A., Selcuk-Kestel, A. S., & Düzgün, H. S. (2017). Analysis of training sample selection strategies for regression-based quantitative landslide susceptibility mapping methods. *Computers & Geosciences*, 104, 62-74. https://doi.org/10.1016/j.cageo.2017.03.022

European Commission. (2023). Proposal for a directive of the European parliament and of the council on soil monitoring and resilience. COM(2023) 416 final. Retrieved March 12, 2025 from https://eur-lex.europa.eu/legal-content/EN/TXT/?uri=celex%3A52023PC0416

European Space Agency (ESA). (2007). *InSAR principles: Guidelines for SAR interferometry processing and interpretation*. ESA Publications. Retrieved February 15, 2025, from https://esamultimedia.esa.int/multimedia/publications/TM-19/TM-19/InSAR_web.pdf

European Space Agency (ESA). (n.d.). Sentinel-1: Copernicus. Retrieved April 2, 2025, from https://www.esa.int/Applications/Observing_the_Earth/Copernicus/Sentinel-1

Fabris, M., Battaglia, M., Chen, X., Menin, A., Monego, M., & Floris, M. (2022). An integrated InSAR and GNSS approach to monitor land subsidence in the Po River Delta (Italy). *Remote Sensing*, 14(21), Article 5578. https://doi.org/10.3390/rs14215578

Ferretti, A., Prati, C., & Rocca, F. (2001). Permanent scatterers in SAR interferometry. *IEEE Transactions on Geoscience and Remote Sensing*, 39(1), 8–20. https://doi.org/10.1109/36.898661

Gaidzik, K., & Ramírez-Herrera, M.T. (2021). The importance of input data on landslide susceptibility mapping. *Scientific Reports*, 11, 98830. https://doi.org/10.1038/s41598-021-98830-y

Galloway, D., & Leake, S. A. (2017). Regional land subsidence caused by the compaction of susceptible aquifer systems accompanying groundwater extraction. In V. P. Singh (Ed.), *Handbook of applied hydrology* (2nd ed., Chapter 56). McGraw-Hill Education.

Guzzetti, F., Reichenbach, P., Cardinali, M., Rossi, M., & Galli, M. (2009). Probabilistic landslide hazard assessment at the basin scale. *Geomorphology*, 112(3-4), 256–267. https://doi.org/10.1016/j.geomorph.2005.06.002

Hanssen, R.F. (2001) *Radar interferometry: data interpretation and error analysis*. Springer Science & Business Media. https://doi.org/10.1007/0-306-47633-9

- Highland, L., & Bobrowsky, P. (2008). *The landslide handbook: A guide to understanding landslides* (USGS Circular 1325). U.S. Geological Survey. ISBN: 978-141132226-4
- Hooper, A., Zebker, H., Segall, P., & Kampes, B. (2004). A new method for measuring deformation on volcanoes and other natural terrains using InSAR persistent scatterers. *Geophysical Research Letters*, 31(23), L23611. https://doi.org/10.1029/2004GL021737
- Huang, G., Du, S., Wang, D. (2023) GNSS techniques for real-time monitoring of landslides: A review. *Satellite Navigation*, 4, Article 5. https://doi.org/10.1186/s43020-023-00095-5
- Ignatenko, V., Dogan, O., Muff, D., Lamentowski, L., Radius, A., Nottingham, M., Leprovost, P., & Seilonen, T. (2022). ICEYE Microsatellite SAR Constellation Status Update: Spotlight Extended Area Mode, Daily Coherent Ground Tracks and Waveform Diversity. *IEEE International Geoscience and Remote Sensing Symposium* 4145-4148. https://doi.org/10.1109/IGARSS46834.2022.9884027
- Intrieri, E., Raspini, F., Fumagalli, A., Lu, P., Del Conte, S., Farina, P., Allievi, J., Ferretti, A., & Casagli, N. (2018). The Maoxian landslide as seen from space: Detecting precursors of failure with Sentinel-1 data. *Landslides*, 15, 123–133. https://doi.org/10.1007/s10346-017-0915-7.
- Japan Aerospace Exploration Agency. (n.d.). ALOS-2 Project / PALSAR-2. Retrieved May 18, 2025, from https://www.eorc.jaxa.jp/ALOS-2/en/about/palsar2.htm
- Jin, S., & Komjathy, A. (2010). GNSS Reflectometry and Remote Sensing: New Objectives and Results. *Advances in Space Research*. 46. 111-117. https://doi.org/10.1016/j.asr.2010.01.014
- Krieger, G., Moreira, A., Fiedler, H., Hajnsek, I., Werner, M., Younis, M. (2007). TanDEM-X: A Satellite Formation for High-Resolution SAR Interferometry. *IEEE Transactions on Geoscience and Remote Sensing*, 45(11) pp. 3317-3341. https://doi.org/10.1109/TGRS.2007.900693
- Kulsoom, I., Hua, W., Hussain, S., Chen, Q., Khan, G., & Shihao, D. (2023). SBAS-InSAR based validated landslide susceptibility mapping along the Karakoram Highway: A case study of Gilgit-Baltistan, Pakistan. *Scientific Reports*, 13(1), Article 30009. https://doi.org/10.1038/s41598-023-30009-z
- Lantmäteriet. (2024). Nu är säsongen för flygfotografering igång (press release). Retrieved April 10, 2025, from https://www.lantmateriet.se/sv/om-lantmateriet/press/nyheter/nu-ar-sasongen-for-flygfotografering-igang/
- Lazecky, M., Canaslan Comut, F., Nikolaeva, E., Bakon, M., Papco, J., Ruiz-Armenteros, A.M., Qin, Y., Sousa, J.J.M. de, Ondrejka, P. (2016). Potenital of Sentinel-1A for nation-wide routine updates of active landslide maps. *ISPRS International Archives of the Photogrammetry, Remote Sensing and Spatial Information Sciences XLI-B7*, 775–781. https://doi.org/10.5194/isprs-archives-XLI-B7-775-2016
- Lee, S. (2019). Current and future status of GIS-based landslide susceptibility mapping: A literature review. *Korean Journal of Remote Sensing*, 35(1), 179–193. https://doi.org/10.7780/kjrs.2019.35.1.12

- Li, S., Xu, W., & Li, Z. (2022). Review of the SBAS InSAR Time-series algorithms, applications, and challenges. *Geodesy and Geodynamics*, 13, 114–126. https://doi.org/10.1016/j.geog.2021.09.007
- Li, J., Xing, X., Ou, J. (2023). Locating and characterizing potential rainfall-induced landslides on a regional scale based on SBAS-InSAR technique. Bulletin of Engineering Geology and the Environment, 82(1), Article 329. https://doi.org/10.1007/s10064-023-03356-4
- Liang, H., Xu, W., Ding, X., Lei, Z., Wu, S. (2021). Urban Sensing with Spaceborne Interferometric Synthetic Aperture Radar. (*eds*) *Urban Informatics. The Urban Book Series*. Springer, Singapore. https://doi.org/10.1007/978-981-15-8983-6 21
- Lu, Z., Kwoun, O., & Rykhus, R. (2007). Interferometric Synthetic Aperture Radar (InSAR): Its past, present and future. *Photogrammetric Engineering and Remote Sensing*, 73(1), 1-14.
- Löfroth, H, Persson, L., Bastani, M., Rodhe, L., Hedfors, J., With, C., Ekström, J., Engdahl, M. (2018). *Tillämpning och utvärdering av metoder för kartläggning av kvicklera*, 2019-01-07, Statens geotekniska institut, Linköping, 2018-12-20.
- Löfroth, H., Fritzson, H., Holmén, M., Lundström, K., Rudebeck, D., Abed, A., Karstunen, M., Jia, Q., & Laue, J. (2024). *Långsamma skred i skiktad siltig jord*. (Report No. 1.1-2208-0778). Statens geotekniska institut.
- Muñoz Sabater, J. (2019): ERA5-Land hourly data from 1950 to present. Copernicus Climate Change Service (C3S) Climate Data Store (CDS). https://doi.org/10.24381/cds.e2161bac
- NASA. (n.d.). SAR: Synthetic Aperture Radar. NASA. Retrieved March 27, 2025, from https://www.earthdata.nasa.gov/learn/earth-observation-data-basics/sar
- Naturvårdsverket. (2024). Digitalisering som stöd för en hållbar förvaltning. Retrieved April 10, 2025, from https://www.naturvardsverket.se/om-miljoarbetet/forskning/miljoforskning/forskningssatsningar-samhalle/digitalisering-som-stod-for-en-hallbar-forvaltning/
- Nikolakopoulos, K. G., Kyriou, A., Koukouvelas, I. K., Tomaras, N., & Lyros, E. (2023a). UAV, GNSS, and InSAR Data Analyses for Landslide Monitoring in a Mountainous Village in Western Greece. *Remote Sensing*, 15(11), Article 2864. https://doi.org/10.3390/rs15112870
- NVE (2014). Bruk av fjernmåling i overvåking av fjellskred og ustabile fjellpartier. Rapport 87-2014. Retrieved May 18, 2025 from https://publikasjoner.nve.no/rapport/2014/rapport2014_87.pdf
- NVE (2015). Overvåking av ustabile fjellpartier i Norge Status og plan. Rapport 122-2015. Retrieved May 18, 2025 from https://publikasjoner.nve.no/rapport/2015/rapport2015 122.pdf
- NVE (2016). Bruk av InSAR til fjernmåling av bevegelser i ustabile fjellpartier Evaluering av ulike sensorer. Rapport 12-2016. Retrieved May 18, 2025 from https://publikasjoner.nve.no/rapport/2016/rapport2016 12.pdf

NVE (2024). Overvåking og klassifisering av fjellskredfare i Norge: Status 2023. Rapport 24-2024. Retrieved May 18, 2025 from https://publikasjoner.nve.no/rapport/2024/rapport2024_24.pdf

Quigley, R.M., (1980). Geology, mineralogy and geochemistry of Canadian soft soils: a geotechnical perspective. *Canadian Geotechnical Journal* 17, 261–285. https://doi.org/10.1139/t80-026

Rao, X. & Tang, Y. (2014). Small baseline subsets approach of DInSAR for investigating land surface deformation along the high-speed railway. *In Proceedings of SPIE - The International Society for Optical Engineering*. https://doi.org/10.1117/12.2069041

Ren, K., Yao, X., Li, R., Zhou, Z., Yao, C., & Jiang, S. (2022). 3D displacement and deformation mechanism of deep-seated gravitational slope deformation revealed by InSAR: A case study in Wudongde Reservoir, Jinsha River. *Landslides*, 19(8), 10. https://doi.org/10.1007/s10346-022-01905-8

Sarkar, S., & Kanungo, D.P. (2004). An integrated approach for landslide susceptibility mapping using remote sensing and GIS. *Photogrammetric Engineering & Remote Sensing*, 70(5), 617–625. https://doi.org/10.14358/PERS.70.5.617

SARmap. (2009). *SAR Guidebook*. Retrieved March 21, 2025 from https://www.sarmap.ch/pdf/SARGuidebook.pdf

SARmap. (2021). *SBAS tutorial* (version 5.6.2). SARmap. Retrieved March 21, 2025 from https://www.sarmap.ch/tutorials/SBAS_Tutorial_562.pdf

Schoning, K., & Lundqvist, L. (2020). Förvaltning och klassificering av geologiska naturvärden i världsarvsområdet Höga kusten (SGU-rapport 2020:39). Sveriges geologiska undersökning. Retrieved April 10, 2025, from https://resource.sgu.se/dokument/publikation/sgurapport/sgurapport202039rapport/s2039-rapport.pdf

SentiWiki. (n.d.). S1 Mission. Copernicus. Retrieved March 27, 2025, from https://sentiwiki.copernicus.eu/web/s1-mission

Shanmugam, G. & Wang, Y. (2015). The landslide problem. *Journal of Palaeogeography*. 4. 109-166, 191–272. https://doi.org/10.3724/SP.J.1261.2015.00071

Shahri, A. A., Spross, J., Johansson, F., & Larsson, S. (2019). Landslide susceptibility hazard map in southwest Sweden using artificial neural network. *Catena*, 183, 104225. https://doi.org/10.1016/j.catena.2019.104225

SLU (2024). Radar och skoglig fjärranalys. Sveriges lantbruksuniversitet. Retrieved May 18, 2025 from https://www.slu.se/institutioner/skoglig-resurshushallning/omraden/skoglig-fjarranalys/arbetsomraden/radar/

Sveriges geologiska undersökning (SGU). (2014). *Tredimensionella jordartsmodeller – programvara och metoder* (SGU Rapport 2014:33). https://resource.sgu.se/dokument/publikation/sgurapport/sgurapport201433rapport/s14 33-rapport.pdf

Sveriges geologiska undersökning (SGU). (n.d.-a). *Jordarter 1:25 000 – 1:100 000: Beskrivning av informationsinnehåll och framställning*. https://resource.sgu.se/dokument/produkter/jordarter-25-100000-beskrivning.pdf

Sveriges geologiska undersökning (SGU). (n.d.-b). Kartvisare – Jorddjup och andra geologiska kartor. https://www.sgu.se/produkter/kartor/

Sveriges geologiska undersökning (SGU). (2016). *Saltvattenavsatta leror i Sverige med potential för att bilda kvicklera* (SGU Rapport 2016:08). https://www.sgu.se/globalassets/produkter/publikationer/tidigare/saltvattenavsatta-leror-i-sverige-med-potential-for-att-bilda-kvicklerasgu-rapport-2016-08.pdf

Sveriges geologiska undersökning (SGU). (2022a). Produktbeskrivning: *Riksöversikt finkorniga jordars skredbenägenhet*. https://resource.sgu.se/dokument/produkter/produktblad/riksoversikt-finkorniga-jordars-skredbenagenhet.pdf

Statens geotekniska institut (SGI). (1984). *Tuveskredet Slutrapport*. Report no11a. https://www.sgi.se/globalassets/publikationer/rapporter/pdf/sgi-r11a.pdf

Statens geotekniska institut (SGI). (2012a). *Skredrisker i Göta älvdalen i ett förändrat klimat: Slutrapport del 2 – Analys och konsekvenser* (Rapport 90:2). https://www.sgi.se/globalassets/publikationer/gota-alvutredningen/gau_slutrapport_del2.pdf

Statens geotekniska institut (SGI). (2012b). *Skredrisker i Göta älvdalen i ett förändrat klimat: Slutrapport del 3 – Kartor* (Rapport 90:3). https://www.sgi.se/globalassets/publikationer/gota-alvutredningen/gau_slutrapport_del3.pdf

Statens geotekniska institut (SGI). (2012c). Naturliga riskområden, skredrisk Göta Älv. Retreived, April 10, 2025, from https://www.geodata.se/geodataexplorer/

Statens geotekniska institut (SGI). (2018). *Metodik för kartläggning av kvicklera: Vägledning* (SGI Publikation 46). Retrieved April 20, 2025 from https://www.sgi.se/globalassets/publikationer/sgi-publikation/sgi-p46.pdf

Statens geotekniska institut (SIG). (2023). *Skredriskkartering i lerjord – Beskrivning av metodik och vägledning för genomförande*. SGI Vägledning 6. Retrieved April 24, 2025 from https://swedgeo.diva-portal.org/smash/get/diva2:1821033/FULLTEXT01.pdf

Statens geotekniska institut. (SGI) (2025). *Kartunderlag om ras, skred och erosion* (SGI Vägledning No. 1, 6th ed.). Retrieved April 20, 2025 from https://www.diva-portal.org/smash/get/diva2:1300126/FULLTEXT03.pdf

Statens geotekniska institut & Myndigheten för samhällsskydd och beredskap (SGI & MSB). (2021). *Riskområden för ras, skred, erosion och översvämning* (SGI Diarienr: 1.1-1907-0483). Retrieved April 13, 2025 from https://www.sgi.se/globalassets/georisker-och-geodata/ru_riskomraden_slutrapport_final_210528_tillganglig_slutversion_ny.pdf

Swedish Meteorological and Hydrological Institute (SMHI). (n.d.). Västergötlands klimat. Retrieved March 15, 2025 from https://www.smhi.se/kunskapsbanken/klimat/klimatet-i-sveriges-landskap/vastergotlands-klimat

Swedish University of Agricultural Sciences. (n.d.). Radar. Skoglig fjärranalys. Retrieved April 17, 2025, from https://www.slu.se/institutioner/skoglig-resurshushallning/omraden/skoglig-

fjarranalys/arbetsomraden/radar/#:~:text=Radar%2C%20eller%20mer%20specifikt%2 0syntetisk,slutligen%20registreras%20av%20en%20antenn

Trafikverket. (2022). Utvärdering av rikstäckande InSAR för transport-infrastruktur (Uppdragsnr. 107 49 71, Version 0.3). https://trafikverket.diva-portal.org/smash/get/diva2:1902286/FULLTEXT01.pdf

USGS. (n.d.). SAR: Synthetic aperture radar. NASA Earth Observing System Data and Information System. Retrieved March 27, 2025 from https://www.earthdata.nasa.gov/learn/earth-observation-data-basics/sar

Yalvac, S. (2020). Validating InSAR-SBAS results by means of different GNSS analysis techniques in medium-and high-grade deformation areas. *Environmental monitoring and assessment*, 192(2), 120. https://doi.org/10.1007/s10661-019-8009-8

Yi, Y., Xu, X., Xu, G., & Gao, H. (2023). Rapid Mapping of Slow-Moving Landslides Using an Automated SAR Processing Platform (HyP3) and Stacking-InSAR Method. *Remote Sensing*, 15(6), 1611. https://doi.org/10.3390/rs15061611

Yu, H., Lan, Y., Yuan, Z., Xu, J., & Lee, H. (2019). Phase unwrapping in InSAR: A review. *IEEE Geoscience and Remote Sensing Magazine*, 7, 40-58. https://doi.org/10.1109/MGRS.2018.2873644

Yunjun, Z., Fattahi, H., Amelung, F. (2019), Small baseline InSAR time series analysis: Unwrapping error correction and noise reduction. *Computers & Geosciences*, 133, 104331. https://doi.org/10.1016/j.cageo.2019.104331

Zhang, J., Gao, B., Huang, H., Chen, L., Li, Y., & Yang, D. (2022). SBAS-InSAR-based landslide susceptibility mapping along the North Lancang River, Tibetan Plateau. *Frontiers in Earth Science*, 10, Article 901889. https://doi.org/10.3389/feart.2022.901889

Zhang, S., Jiang, T., Pei, X., Huang, R., Xu, Q., Xie, Y., ... & Zhi, L. (2022). A new forecasting method for failure time of creep landslide based on nonlinear creep behavior and new pre-warning criterion. *Frontiers in Earth Science*, 10, 1018432. https://doi.org/10.3389/feart.2022.1018432

Data

Statens Geotekniska Institut (SGI). (2001). SGI Varia 512: Inträffade skred, ras och övriga jordrörelser (Skreddatabasen) [Data set- SGI_Skreddatabas_ver2]. Retrieved March 15, 2025 from https://gis.sgi.se/dokument/geodatasezip/

Swedish Geotekniska institut (SGI). (2012). Skredrisker i Göta älvdalen [Data set -skredriskergotaalv]. Retrieved March 15, 2025 from https://gis.sgi.se/dokument/geodatasezip/

Sveriges Geotekniska institut (SGU). (2022). Riksöversikt finkorniga jordars skredbenägenhet [Data set - sgi_10_riskomr]. Retrieved March 15, 2025 from https://gis.sgi.se/dokument/geodatasezip/

Lantmäteriet © (2019) Digital elevation model [Data set - GSD-Höjddata grid 2+]. Retrieved March 12, 2025 from https://www.maps.slu.se

Lantmäteriet © (2016) Railway network [Data set – GSD-Topographic Map Vector, JL Line layer with railways]. Retrieved March 12, 2025 from https://www.maps.slu.se

Sveriges geologiska undersökning (SGU). (2018). Jordarter 1:25 000-1:100 000 [Data set – jordarter_25_100_jg2]. Retrieved March 12, 2025 from https://www.maps.slu.se

University of Nevada, Reno. (n.d.). NGL station pages: GPS net map. Retrieved April 10, 2025, from

https://geodesy.unr.edu/NGLStationPages/gpsnetmap/GPSNetMapMovable.html?latz=57.831&lonz=12.017&zoomlev=11

Valmyndigheten. (n.d.). Röstningskarta för val till riksdag, region och kommun 2022 [Data set – County boundary]. ArcGIS Online. Retrieved May 1, 2025, from https://www.arcgis.com/home/item.html?id=dbae50c537864581895ac2ca2cf5320e

Appendix

Appendix A: InSAR data overview and SBAS quality assessment

Table A1. The SBAS-InSAR processing parameters for the descending and ascending stacks.

Parameter	Descending stack	Ascending stack	
Time period	2017 – 2021	2017 - 2021	
Path	66	146	
Frame	396-399	187-188	
Orbit Direction	Descending	Ascending	
Platform	Sentinel-1A/B	Sentinel-1A/B	
Temporal baseline	6 days (some gaps 12 days)	6 days (some gaps 12 days)	
Perpendicular baseline	200 m	200 m	
Azimuth & Range looks	10x2	10x2	
Seasonal search	March 1 – November 1	March 1 – November 1	
Reference date	2017-03-10	2017-03-03	

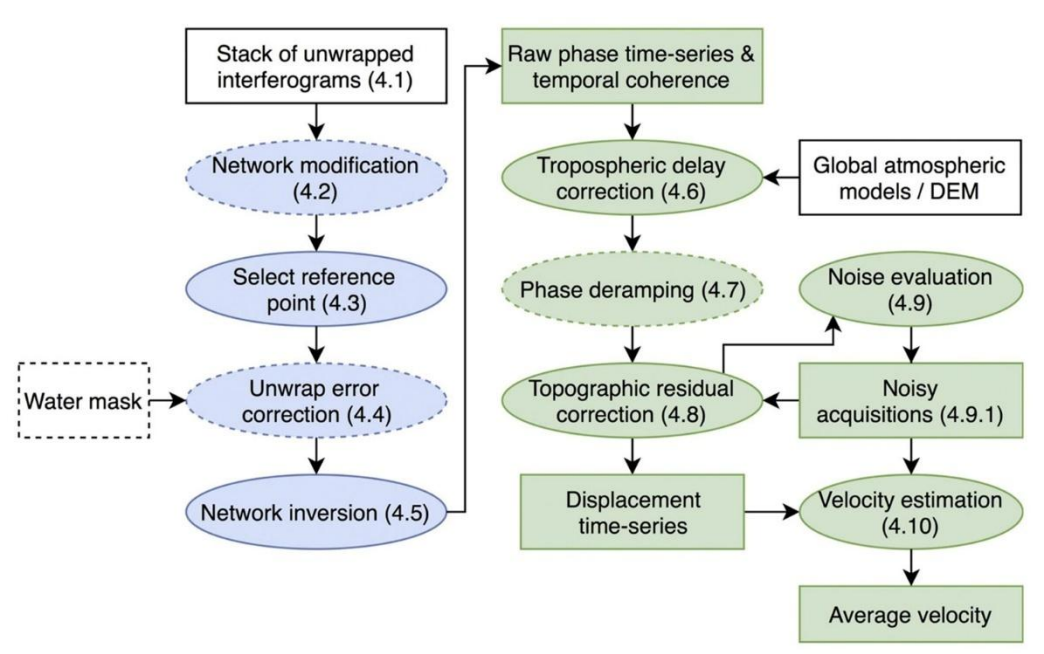


Figure A1. SBAS-InSAR time series workflow from MintPy (figure from Yunjun et al., 2019), showing key steps from network modification and unwrapping error correction to phase corrections and velocity estimation. Steps in blue are performed in the interferogram phase, while green steps are in the time series analysis.

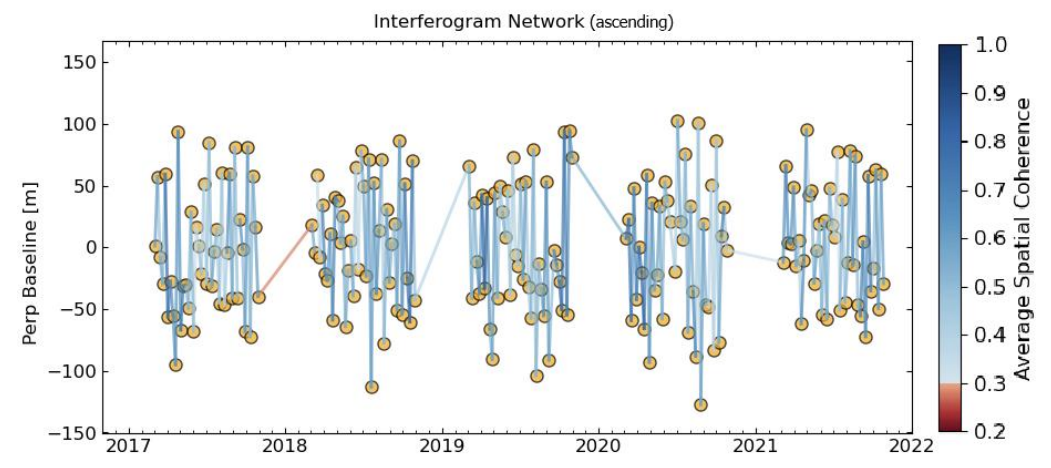


Figure A2. SBAS interferogram network showing temporal and perpendicular baselines for the ascending stack. Color scale indicates average spatial coherence per interferogram. While coherence varies across the stack, all interferograms except 1 remain within the acceptable range for SBAS processing (data range: 0.283-0.837), and none were excluded. The maximum perpendicular baseline is 228.4 m, and the maximum temporal baseline is 132 days. This exceeds the SBAS thresholds set, but was necessary to cover data and seasonal gaps.

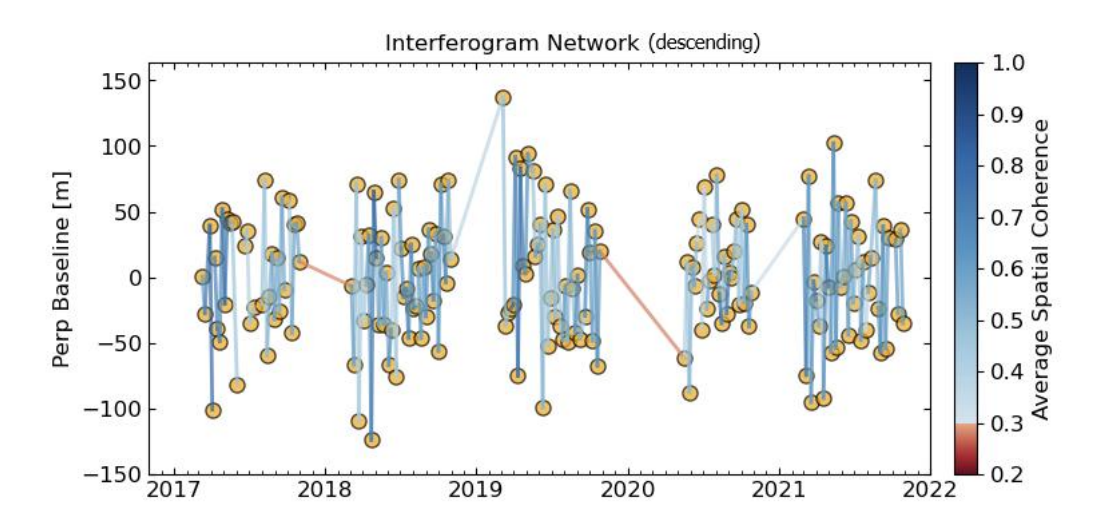


Figure A3. SBAS interferogram network showing temporal and perpendicular baselines for the descending stack. Color scale indicates average spatial coherence per interferogram. Although coherence varies throughout the stack (data range 0.280–0.838), especially during 2020, all interferograms except 2 exceed the commonly used 0.3 threshold, and none were excluded during processing. The maximum perpendicular baseline is 189.48 m and the maximum temporal baseline is 204.0 days. This exceeds the SBAS thresholds set, but was necessary to cover data and seasonal gaps.

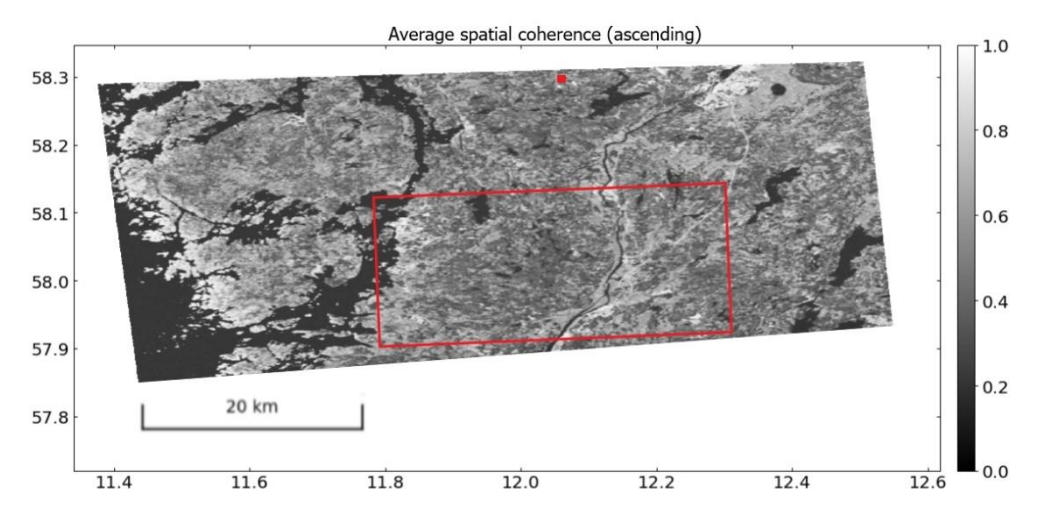


Figure A4. Average spatial coherence map for the ascending track. The grayscale shows the mean spatial coherence for each pixel over the full time series, ranging from low (black) to high (white). The red rectangle outlines the study area. The red dot indicates the reference point used during SBAS processing.

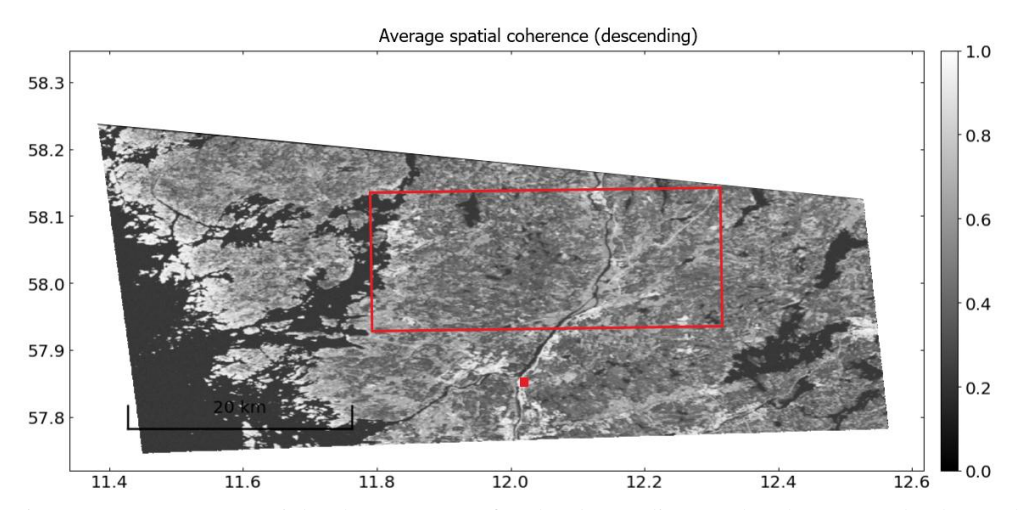


Figure A5. Average spatial coherence map for the descending track. The grayscale shows the mean spatial coherence for each pixel over the full time series. As with figure A4, the red box marks the study area and the red dot shows the reference point location.

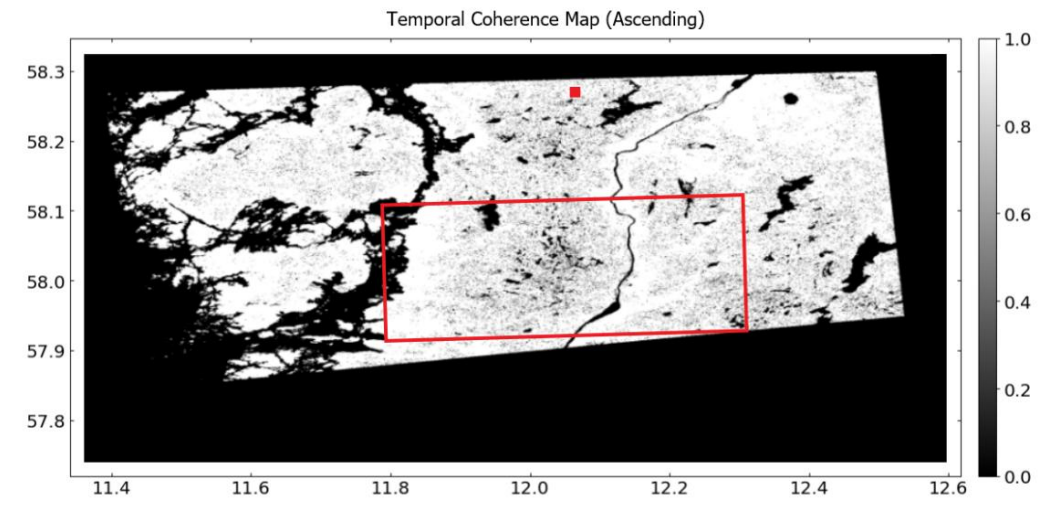


Figure A6. Temporal coherence map for the ascending stack. White tones indicate high temporal coherence suggesting stable phase information across acquisitions. The study area is outlined in red, and the red square shows the reference pixel automatically selected by MintPy for displacement calculations. Coherence is generally high in urban and open terrain, while lower values are found in forested regions.

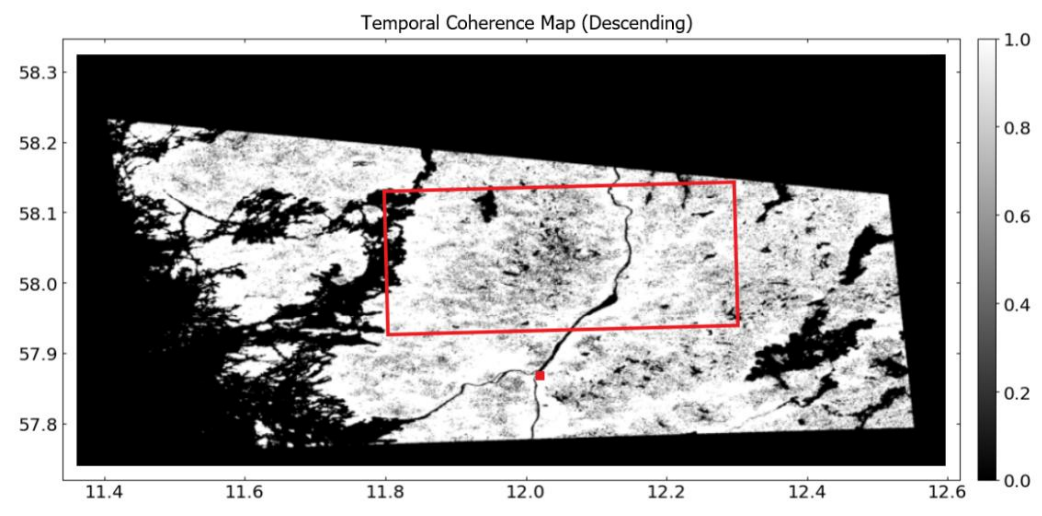


Figure A7. Temporal coherence map for the descending stack. Similar to the ascending track, high coherence is observed across much of the study area (outlined in red), although slightly more variability is seen in the southern and central parts. The red square marks the selected reference point for the descending time series.

Appendix B: Supplementary GIS maps and data

Table B1. Reclassification and selection of high-subsidence soil classes. All original SGU soil classes (by JG2 code) were first merged into a simplified set of classes. Zonal statistics of the SBAS mean velocity were then done for each merged group across the study area. The four categories listed below (Postglacial Fine Sediment, Clay-Silt Sediment, Sandy Sediment, and Glacial Sediment) had the highest mean subsidence rates.

Merged Class	JG2 Code	Original SGU Class Name	Mean LOS Velocity (m/year)
Postglacial fine sediment	19, 22, 17	Postglacial finlera, Postglacial grovlera, Postglacial lera	-0.0184
Clay-silt sediment	9	Svgmsediment, ler-silt; Svimsediment, ler-silt; Svtmsediment, ler-silt	-0.0168
Sandy sediment	28, 31, 10, 95	Postglacial finsand, Postglacial sand, Svgmsediment, sand; Svimsediment, sand, sandig morän (sandig mor, sandig moren, sandig morln, sandig mor\(^1\), sandig mor\(^1\)	-0.0153
Glacial sediment	40, 43, 44, 48, 50, 9010	Glacial lera, Glacial finlera, Glacial grovlera, Glacial silt, Is- sediment (Isglvssediment, Isilvssediment, Istlvssediment), Svgmsediment, grovsilt–finsand; Svtmsediment, grovsilt–finsand	-0.0144

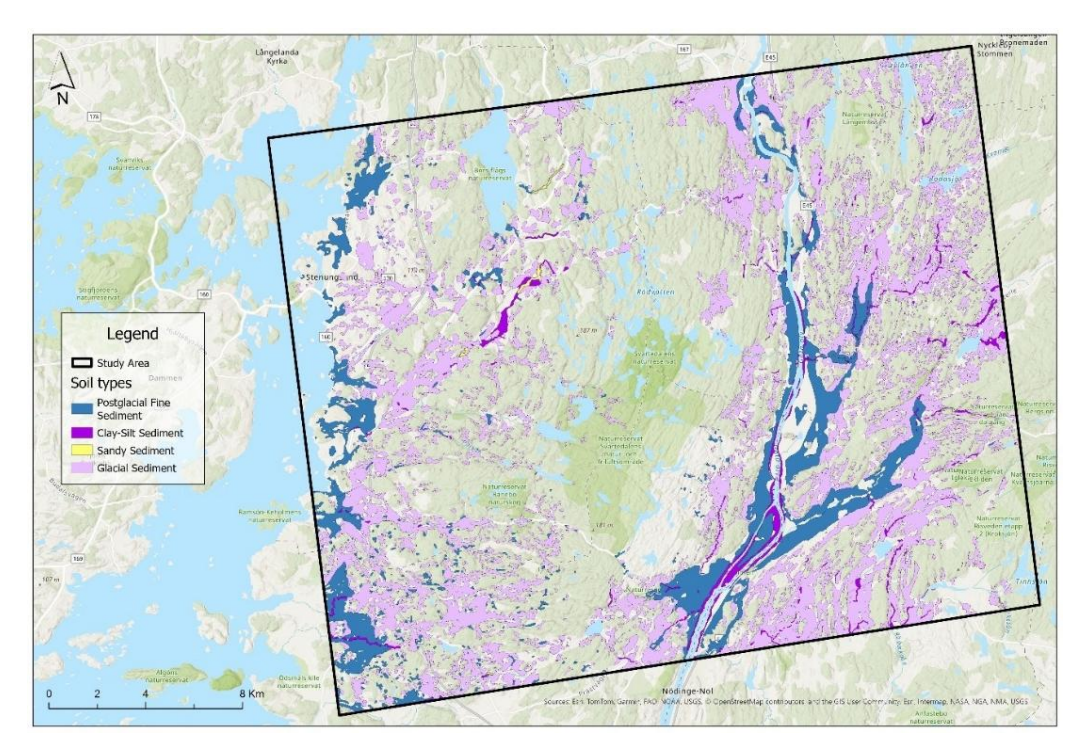


Figure B1. Simplified soil-type map of the Västra Götaland study area, showing only the four merged categories with the highest mean SBAS subsidence rates. The study area is outlined in black. Colors show Postglacial Fine Sediment (mean velocity -0.0184 m/year), Clay-Silt Sediment (-0.0168 m/year), Sandy Sediment (-0.0153 m/year), and Glacial Sediment (-0.0144 m/year).

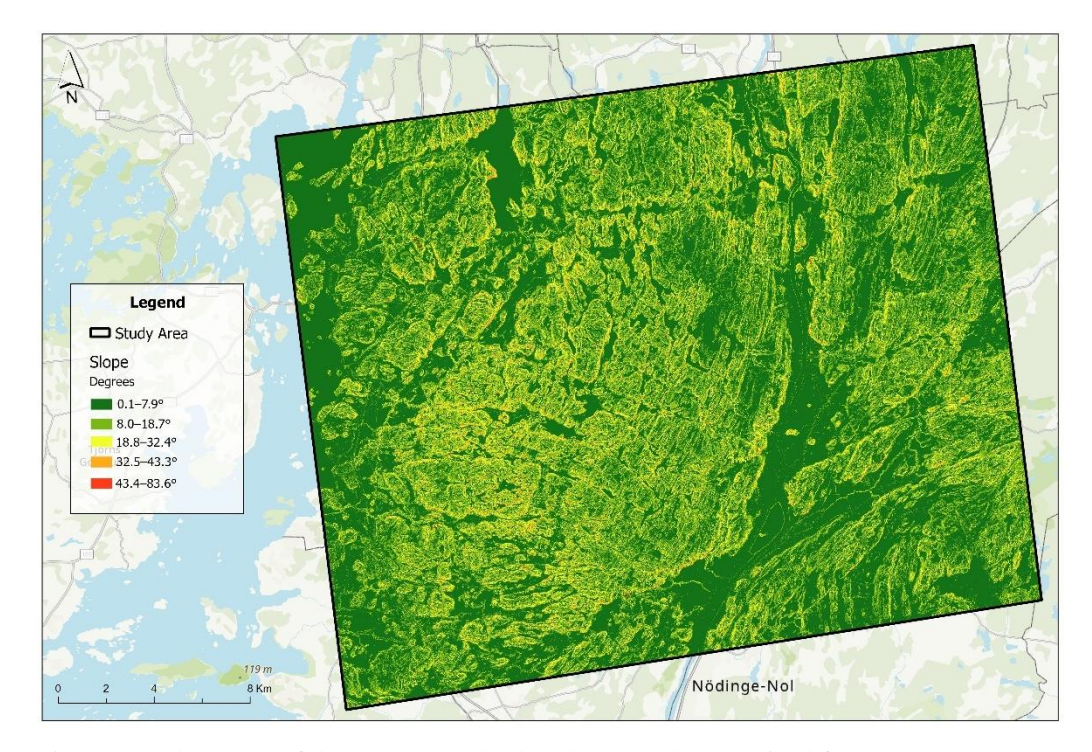


Figure B2. Slope map of the Västra Götaland study area. Slopes derived from a 2 m DEM were grouped into five degree-interval classes shown in the legend. Zonal statistics of SBAS mean velocity show that the gentlest slopes $(0.1–7.9^{\circ})$ experience the greatest subsidence (-0.00975 m/year), followed by $8.0–18.7^{\circ}$ (-0.00618 m/year), $18.8-32.4^{\circ}$ (-0.00527 m/year), $43.4-83.6^{\circ}$ (-0.00459 m/year), and $32.5-43.3^{\circ}$ (-0.00467 m/year), indicating an inverse relationship between slope steepness and average subsidence.

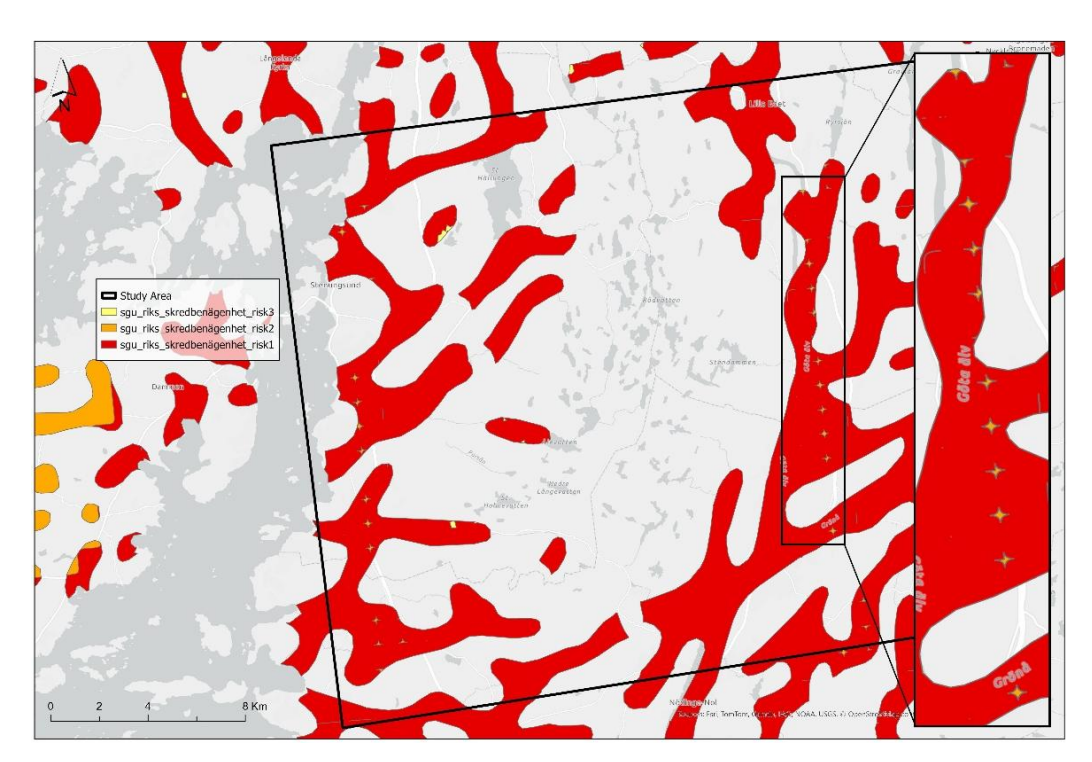


Figure B3. SGU national landslide susceptibility map within the Västra Götaland study area. Significant susceptibility zones (Class 1, red), noticeable susceptibility zones (Class 2, orange), and low susceptibility zones (Class 3, yellow) are displayed with the study-area outline in black. The class "moderate susceptibility to landslides" were not present. The inset (right) highlights the regular, aligned distribution of the Class 2 (orange) zones.